



ACADEMIC
PRESS

Available online at www.sciencedirect.com

SCIENCE @ DIRECT®

Journal of Solid State Chemistry 176 (2003) 338–374

JOURNAL OF
SOLID STATE
CHEMISTRY

<http://elsevier.com/locate/jssc>

Ground- and excited-state properties of inorganic solids from full-potential density-functional calculations

P. Ravindran,* R. Vidya, P. Vajeeston, A. Kjekshus, and H. Fjellvåg

Department of Chemistry, University of Oslo, Box 1033 Blindern, N-0315 Oslo, Norway

Received 17 January 2003; received in revised form 3 April 2003; accepted 10 April 2003

Abstract

The development in theoretical condensed-matter science based on density-functional theory (DFT) has reached a level where it is possible, from “parameter-free” quantum mechanical calculations to obtain total energies, forces, vibrational frequencies, magnetic moments, mechanical and optical properties and so forth. The calculation of such properties are important in the analyses of experimental data and they can be predicted with a precision that is sufficient for comparison with experiments. It is almost impossible to do justice to all developments achieved by DFT because of its rapid growth. Hence, it has here been focused on a few advances, primarily from our laboratory. Unusual bonding behaviors in complex materials are conveniently explored using the combination of charge density, charge transfer, and electron-localization function along with crystal-orbital Hamilton-population analyses. It is indicated that the elastic properties of materials can reliably be predicted from DFT calculations if one takes into account the structural relaxations along with gradient corrections in the calculations. Experimental techniques have their limitations in studies of the structural stability and pressure-induced structural transitions in hydride materials whereas the present theoretical approach can be applied to reliably predict properties under extreme pressures. From the spin-polarized, relativistic full-potential calculations one can study novel materials such as ruthenates, quasi-one-dimensional oxides, and spin-, charge-, and orbital-ordering in magnetic perovskite-like oxides. The importance of orbital-polarization correction to the DFT to predict the magnetic anisotropy in transition-metal compounds and magnetic moments in lanthanides and actinides are emphasized. Apart from the full-potential treatment, proper magnetic ordering as well as structural distortions have to be taken into account to predict correctly the insulating behavior of transition-metal oxides. The computational variants LDA and GGA fail to predict insulating behavior of Mott insulators whereas electronic structures can be described correctly when correlation effects are taken into account through LDA + U or similar approaches to explain their electronic structures correctly. Excited-state properties such as linear optical properties, magneto-optical properties, XANES, XPS, UPS, BIS, and Raman spectra can be obtained from accurate DFT calculations.

© 2003 Elsevier Inc. All rights reserved.

PACS: 71.20.-b; 71.20.Be; 71.20.Lp; 75.50.Cc

1. Introduction

Since its introduction in the 1960s [1,2], density-functional theory (DFT) has evolved into a powerful tool that is widely used in solid-state chemistry and materials science for the calculation of electronic, magnetic, and structural properties of solids. This theory has been remarkably successful in predicting, reproducing, and/or explaining a wide variety of materials ground-state phenomena. Excited states, on

the other hand, are not contained within the framework of DFT, and are generally speaking much more demanding. However, it is these properties that are probed by spectroscopic methods, and utilized for technological applications. Therefore, it is necessary to develop and test ab initio techniques that are capable of predicting excited-state properties equally reliable as, for instance, DFT does for the ground-state properties. This review aims at giving examples of the recent developments in the calculation of ground- and excited-state properties of crystalline solids based on the DFT. The examples are chosen from the work of the present authors. A short summarizing account of theoretical perspectives are given in the introduction to each subsection.

*Corresponding author.

E-mail address: ponniah.ravindran@kjemi.uio.no (P. Ravindran).

URL: <http://folk.uio.no/ravi>.

2. Ground-state properties

2.1. Unusual bonding in metal hydrides

Classically, the chemical bonding in solids are classified as ionic, covalent, and metallic. However, the bonding in a real system is certainly a mixture characteristic of the three classes. The results of theoretical electronic-structure calculations can be easily used to study the nature of chemical bonds since the calculations refer to the ground-state electronic structure, i.e., the distribution of electrons in the crystal. Traditionally, the distribution of electron bands in reciprocal space or the distribution of states in energy [the density of states (DOS)] helps one to study the bonding in a given material. By analyzing the DOS decomposed according to site and angular momenta, one can distinguish between ionic and covalent bonds in solid systems. The nature of the bonding can be analyzed with several other tools such as valence-charge-density plot, charge-transfer plot, electron-localization function (ELF), and crystal-orbital Hamilton population (COHP); which all can be derived from the electronic structure calculations. In this section we illustrate how the above-mentioned tools can be used to gain insight into the chemical bonding in metal hydrides.

The most attractive aspect of metal hydrides from a technological point of view is their potential use as energy-storage materials. The amount of hydrogen per volume unit in metal hydrides is very high; in some cases higher than in liquid or solid hydrogen, e.g., VH_2 stores more than twice the amount of hydrogen compared with solid H_2 at 4.2 K. It is unfortunate, however, that most metal hydrides are heavy in relation to the amount of hydrogen they contain. FeTiH_2 and LaNi_5H_7 , e.g., only contain 1.9 and 1.6 wt% hydrogen, respectively. Therefore, efforts in hydride research have over the past 25–30 years been concentrated on designing new, or modifying known, intermetallic hydrides to increase the storage capacity and simultaneously adjust their properties to make them capable of delivering hydrogen at useful pressures (>0.1 MPa) and acceptable temperatures (<425 K) [3]. These aspects are particularly important for most mobile applications where hydrogen would be used directly in combustion engines or indirectly via fuel cells.

The search for efficient hydrogen-storage metal hydrides [4] has to some extent been hampered by the mental barriers which empirical rules have put on the thinking. For example, the interstitial hole size which hydrogen is expected to occupy should be >0.40 Å [5]. Switendick [6] observed from a compilation of experimental structure data that the minimum H–H separation in ordered metal hydrides is >2 Å (“the 2-Å rule”). This empirical picture is later [7] supported by

band-structure calculations which ascribe the effect to repulsive interaction generated by the partially charged hydrogen atoms. A practical consequence of this repulsive H–H interaction in metal hydrides is that it puts a limit to the amount of hydrogen which can be accommodated within a given structural framework. So, if H–H separations less than 2 Å would be possible this could open for new efforts to identify potential intermetallics with higher hydrogen-storage capacity. However, there are indeed metal hydrides which do violate “the 2-Å rule” and the origin for such behavior has been identified [8].

RNiIn ($R = \text{La, Ce, Pr, and Nd}$) crystallizes in the ZrNiAl -type structure and can formally be considered as a layered arrangement with a repeated stacking of two different planar nets of composition $R_3\text{Ni}_2$ and NiIn_3 along [001] of the hexagonal unit cell. If the hydrides of these materials obey the hole-size demand and “the 2-Å rule” one would expect H to occupy the interstice formed by the trigonal bipyramid $R_3\text{Ni}_2$ ($2d$ site of space group $P\bar{6}2m$). However, proton-magnetic-resonance (PMR) studies suggest [9,10] that H occupies both the $4h$ and $6i$ sites or either of them with H–H distances in the range 1.5–1.8 Å. Recent powder X-ray and neutron-diffraction studies [11] on $\text{RNiInD}_{1.333-x}$ (ideally $R_3\text{Ni}_3\text{In}_3\text{D}_4$) show that deuterium occupies the $4h$ site located on three-fold axis of $R_3\text{Ni}$ tetrahedra that share a common face to form trigonal bipyramids (see Fig. 1 in Ref. [8]). This configuration gives rise to extraordinary short H–H separations of around 1.6 Å [11]. As the diffraction techniques generally determine the average structure, neglect of partial H-site occupancies and local lattice distortions may lead one to conclude with shorter H–H separations than actually present in the real structure [12]. Hence, it is of interest to perform structural optimization theoretically.

All calculations relate to ideal and fully saturated hydrides with composition $R_3T_3\text{In}_3\text{H}_4$ ($\text{RTInH}_{1.333}$; $R = \text{La, Ce, Pr or Nd, } T = \text{Ni, Pd or Pt}$). For (trivalent) R the $4f$ electrons were treated as core electrons (except for La; $4f$). As Ce- $4f$ electrons are known to take different valence states in intermetallic compounds, different possibilities [13] for the valence states of Ce were considered in both the hydrides and intermetallic phases during the structural optimization. For this optimization all atom positions were relaxed by force minimization and equilibrium c/a and volume were obtained by total-energy minimization. Optimized structural parameters for the Ce compounds are in good agreement with experimental values only when Ce are assumed to be in the trivalent state. The calculated equilibrium lattice parameters and the changes between the intermetallic and corresponding hydride phases are given for selected compounds along with experimental parameters in Table 1.

Table 1

Calculated lattice parameters (a and c in Å) and c/a for $\text{LaTiInH}_{1.333}$ and relative variation in unit-cell dimensions (in %) consequent on hydrogenation from RTIn to $\text{RTInH}_{1.333}$, experimental values from Ref. [11]

Compound	a		c		c/a		$\Delta a/a$		$\Delta c/c$		$\Delta V/V$	
	Theor.	Exp.	Theor.	Exp.	Theor.	Exp.	Theor.	Exp.	Theor.	Exp.	Theor.	Exp.
$\text{LaNiInH}_{1.333}$	7.2603	7.3810	4.5522	4.6489	0.6270	0.6399	-3.969	-2.76	14.02	14.8	5.14	8.54
$\text{LaPdInH}_{1.333}$	7.3501	—	4.8112	—	0.6546	—	-5.42	—	16.64	—	4.33	—
$\text{LaPtInH}_{1.333}$	7.7274	—	4.6903	—	0.6070	—	-0.04	—	13.98	—	14.00	—
$\text{CeNiInH}_{1.333}$	7.4536	7.2921	4.4871	4.6238	0.6020	0.6341	-1.68	-3.21	12.72	16.3	8.97	8.98
$\text{PrNiInH}_{1.333}$	7.3783	7.260	4.4726	4.560	0.6062	0.6281	-2.85	-3.73	13.93	15.4	7.52	7.01
$\text{NdNiInH}_{1.333}$	7.2408	7.2255	4.5560	4.5752	0.6292	0.6332	-3.72	-3.92	16.75	16.5	7.60	7.53

Table 2

Calculated interatomic distances (in Å) for $\text{RTInH}_{1.333}$

Compound	$R-H$		$T-H$		$H-H$	
	Theor.	Exp.	Theor.	Exp.	Theor.	Exp.
$\text{LaNiInH}_{1.333}$	2.379	2.406	1.489	1.506	1.573	1.635
$\text{LaPdInH}_{1.333}$	2.373	—	1.644	—	1.523	—
$\text{LaPtInH}_{1.333}$	2.475	—	1.618	—	1.454	—
$\text{CeNiInH}_{1.333}$	2.427	2.371	1.457	1.508	1.572	1.606
$\text{PrNiInH}_{1.333}$	2.387	—	1.492	—	1.487	—
$\text{NdNiInH}_{1.333}$	2.350	2.350	1.493	1.506	1.492	1.562

In general, the calculated lattice parameters are in good agreement with the experimental values, and the small differences found may partly be attributed to hydrogen non-stoichiometry (around 10%) in the experimental studies. The hydrogen-induced lattice expansion is strongly anisotropic (Table 1); a huge expansion along [001] ($\Delta c/c = 14-20\%$) and a smaller intra-layer contraction ($-\Delta a/a = 0-5.8\%$). The calculated cohesive energy and heat of formation for the hydrides are larger than for the corresponding intermetallic phases indicating that it might be possible to synthesize all these hydrides. The electronic structure studies show that all considered phases are in the metallic state consistent with experimental findings. Calculated $R-H$, $T-H$, and $H-H$ distances are given in Table 2 along with experimentally available values.

An interesting observation is that all $\text{RTInH}_{1.333}$ materials have unusually short $H-H$ distances. Two explanations have been proposed. Pairing of the hydrogen atoms (either by molecular H_2 -like bonding or by bonding mediated by the intermediate T atom) has been advanced to explain the anomalous PMR spectrum of $\text{CeNiInH}_{1.0}$ [9]. The second explanation focuses on the significantly shorter La-La distance in $\text{LaNiInH}_{1.333}$ than in closely related phases [11], whereby the La atoms (generally R) may act as a shielding that compensates the repulsive $H-H$ interaction.

In order to evaluate these possibilities we have calculated the total energy for (hypothetical) $\text{LaPtInH}_{1.333}$ as a function of $H-H$ separation according

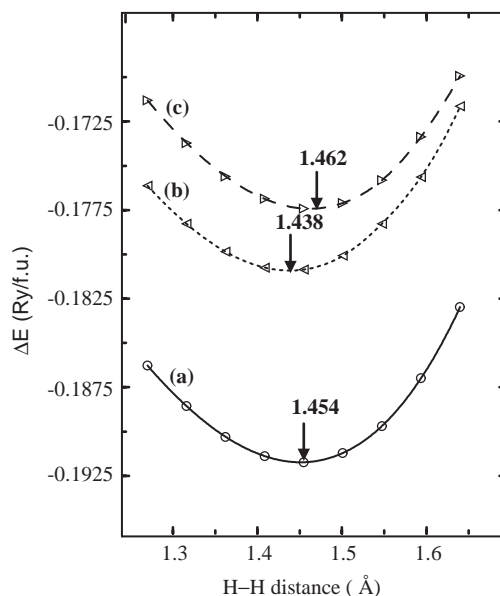


Fig. 1. Total energy vs. $H-H$ distance in $\text{LaPtInH}_{1.333}$. (a) All atoms except H are fixed at their equilibrium positions. (b) La atoms are moved 0.08 \AA out of their equilibrium position toward H. (c) La atoms are moved 0.08 \AA out of their equilibrium position away from H.

to three different scenarios: (1) Keeping La, Pt, and In fixed in their equilibrium positions, (2) moving La 0.08 \AA out of the equilibrium position toward H, and (3) moving La 0.08 \AA out of the equilibrium position away from H. The obtained results are illustrated in Fig. 1. When La, Pt, and In are in their optimized equilibrium position, the equilibrium $H-H$ separation is 1.454 \AA . This scenario corresponds to a lower total energy than the two alternatives. For scenario 2 we obtain a shorter $H-H$ separation (1.438 \AA) than for the ground-state configuration, and for scenario 3 a correspondingly larger separation (1.462 \AA).

As the total-energy curves increase steadily on reduction of the $H-H$ separations, the possibility of stabilization of hydrogen in the form of molecular H_2 -like units seems completely ruled out. The total energy increases drastically also for increased $H-H$ separation beyond the equilibrium value. This is due to

increasing repulsive T – H interaction and decreasing attractive H – H interaction. The considerable changes in the equilibrium H – H distance on R displacement indicate that R in the R_3T_2 trigonal bipyramidal configuration acts as a shielding that to some extent compensates the repulsive H – H interactions. When the R – H separation is reduced the H atoms are allowed to approach each other more closely.

Owing to charge transfer from metal to hydrogen the repulsive H – H interaction in metal hydrides are generally larger than that within the H_2 molecule and this may be the physical basis for “the 2-Å rule”. Another example of violation of “the 2-Å rule” is found for Th_2AlH_4 [14], but here the minimum H – H separation (1.945 Å) within the Th_5 trigonal bipyramids is much larger than the bond distance in the H_2 molecule and the H – H separations in $RTInH_{1.333}$. To gauge the bond strength we have used COHP [15] analyses, as is implemented in the TBLMTO-47 package [16,17]. COHP, which is the Hamiltonian population weighted DOS, is identical with the crystal-orbital-overlap population. If COHP is negative, it indicates bonding character, whereas positive COHP indicates antibonding character. Results from such COHP analyses for $LaNiInH_{1.333}$ are shown in Fig. 2 for all possible interactions within a 3.5 Å range. This illustration shows that the valence band (VB) comprises mainly bonding orbitals and that antibonding orbitals are found ~ 3 eV above the Fermi level (E_F). In order to quantify the bonding interaction between the constituents in the $RTInH_{1.333}$ series the integrated

crystal-orbital Hamilton population (ICOHP) were calculated. For example, the ICOHP values up to E_F for $LaNiInH_{1.333}$ are -3.44 , -0.14 , -0.72 , -0.85 , -0.86 , -1.21 , and -0.61 eV for $Ni(2c)$ – H , H – H , La – H , $Ni(2c)$ – In , La – $Ni(1b)$, $Ni(1b)$ – In , and $Ni(2c)$ – La , respectively. This indicates that the strongest bonds are between $Ni(2c)$ and H . Another important observation is that the bonding interaction between the hydrogens is small, which further confirms that the short H – H separation in these materials are not rooted in hydrogen pairing or formation of H_2 -like molecular units.

As measured by ICOHP, the bonding interaction $Ni(2c)$ – In is reduced upon hydrogenation (from around -1.20 to -0.85 eV). The bonding ICOHP values for the short H – H separations are very small, around -0.04 eV, thus supporting the already advanced inference that there is no significant covalent bonding interaction between the H atoms [18]. The low ICOHP value reflects the fact that both bonding and antibonding states are present below E_F , but even if one takes into account only the bonding states, the ICOHP remains low [-0.14 to -0.23 eV, which is much smaller than ICOHP for $Ni(2c)$ – H]. Hence, both COHP and charge-density analyses agree that the H – H interaction is considerably smaller than the $Ni(2c)$ – H interaction. This therefore disagrees with NMR findings for $CeNiInH_x$ and $PrNiInH_x$ [9,10,19] which conclude that $H\cdots H$ pairing is the main reason for the unusually short H – H separation in these hydrides. On the basis of neutron-diffraction results [11] it has been speculated that the H – H interaction is shielded by the R – R interaction. However, our COHP study shows that the R – R interaction is only ca. -0.62 eV in ICOHP which is 5–6 times smaller than for the $Ni(2c)$ – H interaction and closer to the bond strength for R – H and R – $Ni(2c)$.

In order to substantiate this observation further we have calculated the valence-charge-density distribution in (100) of $LaNiInH_{1.333}$ (Fig. 3a). From this figure, it is apparent that Ni and H form a NiH_2 molecule-like structural subunit. Moreover, Fig. 3a demonstrates that there is no substantial charge-density distributed between the H atoms. The charge transfer (the difference in the electron density of the compound and that of constituent atoms superimposed on the lattice grid) for $LaNiInH_{1.333}$ within (100) depicted in Fig. 3b shows that electrons are transferred from La , In , and Ni to the H site. So, there is a considerable ionic-bonding component between H and the metal-host lattice. The transferred electrons from the metal-host lattice to the H_2 -like subunit of the structure enter the antibonding σ^* levels and gives rise to repulsive interaction. This repulsive interaction between the negatively charged H atoms could explain why the H – H separation in these materials are larger than that in the H_2 molecule. If there had been strong covalent bonding between Ni and H one would have expected a significant (positive) value

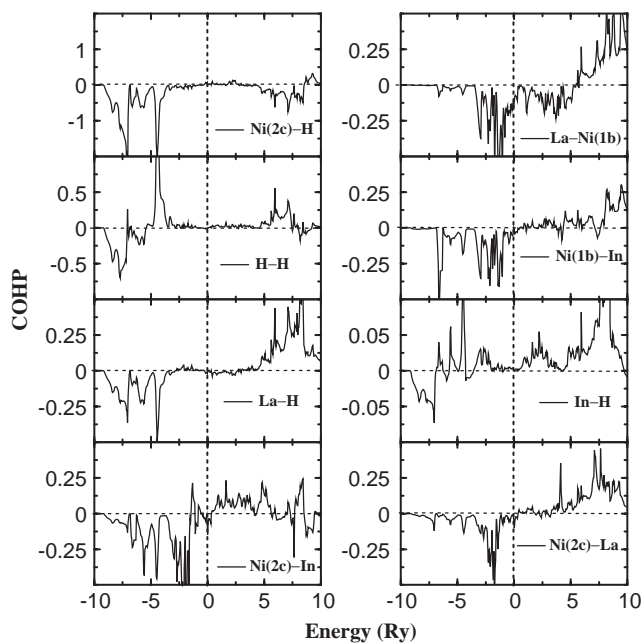


Fig. 2. COHPs for $LaNiInH_{1.333}$; referring to the short distances corresponding to the combinations $Ni(2c)$ – H , H – H , La – H , $Ni(2c)$ – In , La – $Ni(1b)$, $Ni(1b)$ – In , In – H , and $Ni(2c)$ – La .

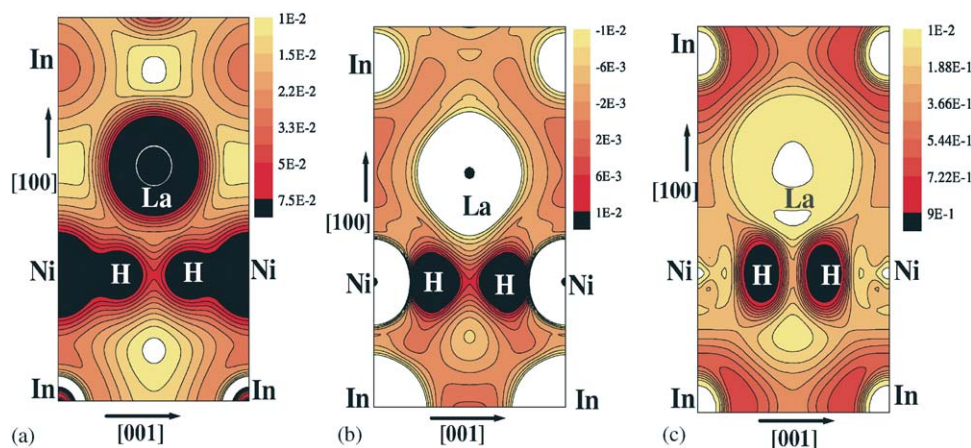


Fig. 3. (a) Total charge density (in e/a.u.³), (b) charge transfer, and (c) electron-localization function for LaNiInH_{1.333} in the (100) plane. Origin is shifted to (1/3, 0, 0).

of charge transfer distributed between these atoms (contributed by both atoms). The absence of such a feature rules out this possibility.

The ELF is an informative tool to distinguish different bonding interactions in solids [20] and the ELF for LaNiInH_{1.333} in (100) is given in Fig. 3c. The large value of the ELF at the H site indicates strongly paired electrons with local bosonic character. Another manifestation of covalent bonding between Ni and H should have been paired electron distribution between these atoms. The negligibly small ELF between Ni and H indicates that the probability of finding parallel spin electrons close together is rather high (correspondingly small for antiparallel spin pairs) in this region, thus confirming metallic bonding consistent with the result obtained from the charge-transfer analysis. The detailed analysis show that delocalized metallic Ni(2*c*)-*d* electrons occupy this region. Even though the charge distribution between Ni and H looks like typical covalent bonding, the charge transfer and ELF analyses clearly show that the electron distribution between Ni and H has parallel spin alignment and is solely coming from the Ni site. Hence, the chemical bonding between Ni and H is dominated by metallic components with a considerable ionic weight. The partial DOS analyses also show that the H-*s* states are well separated from the Ni-*d* states in the whole VB, indicating the presence of ionic bonding between Ni and H. Due to the repulsive interaction between the negatively charged H electrons, the ELF contours are not spherically shaped but polarized toward La and In. The localized nature of the electrons at the H site and their polarization toward La and In reduce significantly the H–H repulsive interaction and this can explain the unusually short H–H separation in LaNiInH_{1.333}. The ELF between the H atoms takes a significant value of 0.35. Considering the small charge density, this indicates a weak metallic type of interaction between the hydrogen atoms.

The experimental and theoretical studies show highly anisotropic lattice expansion on hydrogenation of RNiIn. According to the crystal structure of RNiIn, the possible positions for hydrogen accommodation are 6*i* and 4*h* sites, but from a hole size point of view 4*h* is more favorable than 6*i* (ca. 0.4 Å for 4*h* vs. ca. 0.34 Å for 6*i*). The optimized atom positions of the hydrogenated compounds show that the structural deformation does not lead to any substantial rearrangement of the metal atoms in the basal plane. None of the atoms in the hydrides are significantly shifted in *x*, *y* coordinates from those of the corresponding intermetallics. This may be because all atoms are bonded strongly (according to the COHP analyses) in the *ab* plane, hence there would be insufficient room for H in this plane. When H occupies the 4*h* site the atoms try to rearrange themselves to have a minimum energy configuration. Hence, the only possibility is to expand the lattice along [001]. The charge-density study clearly indicates formation of H–Ni–H linear units along [001], which in turn lead to expansion along *c*. The charge-transfer plot shows that as a consequence of the formation of the hydride phase, there occurs some charge transfer from the electron-rich metal atoms to the H site which in turn lead to contraction within *ab* plane, viz. explaining the anisotropic lattice changes upon hydrogenation.

2.2. High-pressure studies on metal hydrides

As a result of the rapid development in diamond-anvil cell (DAC) techniques, a broad range of studies of physical and chemical properties of solids can now be conducted in situ at high pressures up to the Mbar range. Ruoff et al. [21] claimed to have reached experimentally a maximum pressure of 4.16 Mbar which is well above the estimated pressure at the center of the Earth (3.6 Mbar) [22]. The application of pressure provides an ideal means to carefully tune electronic,

magnetic, structural, and vibrational properties for a wide range of applications. Total-energy calculations based on the DFT allow us to derive free energies, and hence the energetics of different structures for a given solid as a function of pressure. Extreme pressures provide a fertile ground for the formation of new materials, evidenced by the new phase transitions observed in scores of materials studied to date, and the appearance of entirely new classes of materials [23,24]. As theory has no limitations for studies of properties of materials at high pressures, one can use this tool to explore the multi-Mbar range. For hydride materials experimental high-pressure studies are hampered by the small scattering cross section of hydrogen to X-rays, poor output intensity from DAC measurements (compared to normal X-ray-diffraction measurements) and various challenges connected with the use of neutron-diffraction techniques. Hence, computational means are very favorable approaches to high-pressure behaviors of hydrides.

The utilization of high-pressure technology has made considerable progress both in experimental and theoretical studies of hydrogen-storage materials. Magnesium is an attractive material for hydrogen-storage applications because of its light weight, low manufacture cost, and high hydrogen-storage capacity (7.66 wt.%). On the other hand, owing to its high operation temperature (pressure plateau of 1 bar at 525 K) and slow absorption kinetics, practical applications of magnesium-based alloys have been limited. However, it has recently been established that improved hydrogen-absorption kinetics can be achieved by means of reduced particle size and/or addition of transition metals to magnesium and magnesium hydrides [25]. γ -MgH₂ often occurs as a by-product in high-pressure synthesis of technologically important metal hydrides like Mg₂NiH₄. Hence, a complete characterization of γ -MgH₂, in particular knowledge about its stability at high pressures, is desirable. As high-pressure X-ray-diffraction studies have difficulties to identify the exact position of hydrogen atoms owing to its very low scattering cross section, the theoretical identification of the hydrogen positions would be of great values.

α -MgH₂ crystallizes with TiO₂-r-type (r = rutile) structure at ambient pressure and low temperature [26]. At higher temperatures and pressures tetragonal α -MgH₂ transforms into orthorhombic γ -MgH₂. Recently Bortz et al. [27] solved the crystal structure of γ -MgH₂ (α -PbO₂ type) on the basis of powder neutron-diffraction data collected at 2 GPa. The α - to γ -MgH₂ transition pressure is not yet known. In addition to the experimentally identified α - and γ -modifications of MgH₂, calculations have been performed for several other possible [28] types of structural arrangements for MgH₂ (details in Ref. [29]). The generalized gradient approximation (GGA) [30] has been used to obtain

accurate exchange and correlation energies for the structural arrangements considered. The structures are fully relaxed for all volumes considered using force as well as stress minimization. Experimentally established structural data were used as input for the calculations when available. The Vienna ab initio simulation package projected-augmented plane-wave (VASPPAW) method was used for the total-energy calculations to establish phase stability and transition pressures. In order to avoid ambiguities regarding the free-energy results the same energy cutoff and a similar **k**-grid density for convergence were used; 500 **k** points in the whole Brillouin zone for α -MgH₂ and a similar density of **k** points for the other structural arrangements. The PAW pseudo potentials [31] were used for all VASP calculations, a demand of at least 0.01 meV/atom for the self-consistent convergence of the total energy, and a plane-wave cutoff of 400 eV.

The calculated total energy vs. volume relation for the different alternatives considered are shown in the Fig. 4. The equilibrium volumes (for α - and γ -MgH₂) are within 1% of the experimental values indicating that the theoretical calculations are reliable. The calculated positional parameters are also in excellent agreement with the experimental data. The calculated values for the bulk modulus (B_0) vary between 44 and 65 GPa for the

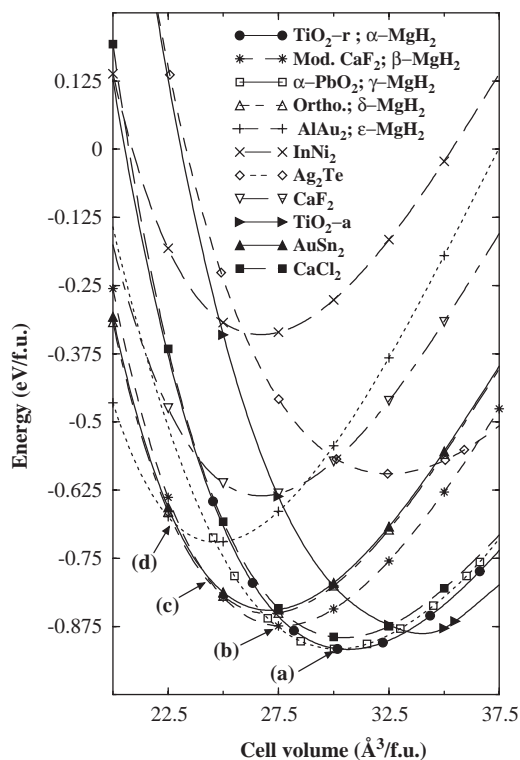


Fig. 4. Calculated cell volume vs. total-energy relations for MgH₂ in actual and possible structural arrangements as obtained according to the PAW method. The arrows marked by (a), (b), (c), and (d) indicate structural transition point.

various structural arrangements. Among the eleven possibilities considered the Ag_2Te -type structure leads to the smallest B_0 value and the AlAu_2 type to the highest.

The calculated transition pressure for the α - to γ - MgH_2 conversion is 0.387 GPa (Fig. 5) and as the free energy of the two modifications is nearly the same at the equilibrium volume (Fig. 4), it is only natural that these phases coexist in a certain volume range [27]. Structurally α - and γ - MgH_2 are also closely related, both comprising Mg in an octahedral coordination of 6 H which in turn are linked by edge sharing in one direction and by corner sharing in the two other directions. The chains are linear in tetragonal α - MgH_2 and run along the four-fold axis of its TiO_2 -r-type structure, while they are zig-zag shaped in γ - MgH_2 and run along a two-fold screw axis of its orthorhombic α - PbO_2 -type structure. The octahedra in γ - MgH_2 are strongly distorted. The pressure-induced α -to- γ transition involves reconstructive (viz. bonds are broken and re-established) rearrangements of the cation and anion sublattices. The occurrence of a similar phase transition in PbO_2 suggests that thermal activation or enhanced shear is of importance [32].

The subsequent phase transition from γ - to β - MgH_2 occur at 3.84 GPa. Bortz et al. [27] found no evidence for the formation of such a β modification up to 2 GPa, whereas Bastide et al. [26] found that at higher pressure (4 GPa) and temperature (923 K) there occurs a new phase (viz. β in accordance with our findings). However, the H positions are not yet determined experimentally and hence its optimized structural parameters [29]

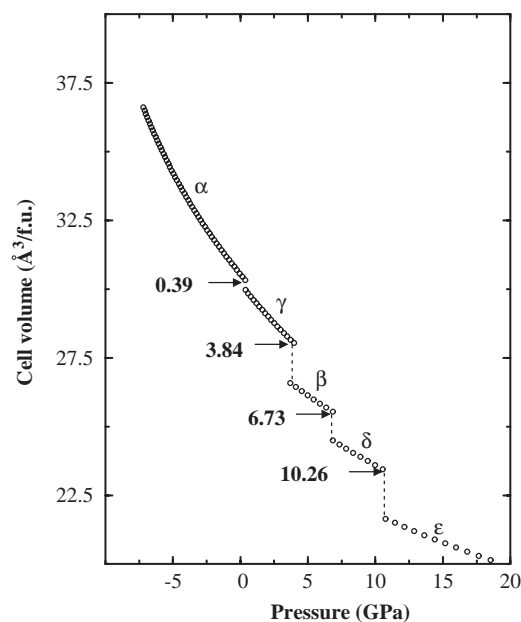


Fig. 5. Pressure vs. cell volume relation for MgH_2 . Phase-transition regions for different modifications are indicated by arrows.

should be of particular interest. The volume shrinkage at the transition point is $1.45 \text{ \AA}^3/\text{f.u.}$ On further increase of the pressure to around 6.7 GPa, β - MgH_2 is predicted to transform into δ - MgH_2 with a volume shrinkage of $1.1 \text{ \AA}^3/\text{f.u.}$ In the pressure range 6.7–10.2 GPa the structural arrangements β - MgH_2 , AuSn_2 -type, and δ - MgH_2 are seen to lie within a narrow energy range of some 10 meV (Fig. 4). This closeness in energy suggests that the relative appearance of these modification will be quite sensitive to, and easily affected by, other external factors like temperature and remnant lattice stresses. A transformation to ϵ - MgH_2 (AlAu_2 -type) is clearly evident from Fig. 4 with a volume change of $1.7 \text{ \AA}^3/\text{f.u.}$ at the transition point (Fig. 5). It is interesting to note that similar structural transition sequences are reported for transition-metal oxides like HfO_2 [28]. Recently, the AlAu_2 -type structure of TiO_2 (synthesized at pressure above 60 GPa) has been shown [33] to exhibit an extremely high bulk modulus (431 GPa) and hardness (38 GPa). The calculations predict that it should be possible to stabilize MgH_2 in the AlAu_2 -type structure (a soft material with $B_0 = 65 \text{ GPa}$) above 10.26 GPa.

The calculated cell-volume difference per formula unit between the involved phases at their equilibrium volume relative to the α -phase is 0.497 (for γ), 2.94 (for β), 3.60 (for δ), and 5.96 (for ϵ) $\text{ \AA}^3/\text{f.u.}$, which is approximately 1.6%, 9.5%, 11.8%, and 19.5%, respectively, smaller than the equilibrium volume of the α -phase. The energy difference between the α -phase and the γ , β , δ , and ϵ phases at the equilibrium volume is 0.81, 43, 66, and 197 meV/f.u., respectively, which is considerably smaller than for similar types of phase transitions in transition-metal dioxides [28]. The known stabilization of the high-pressure phase of TiO_2 by using high-pressure–high-temperature synthesis [33] indicates that it may be possible to stabilize high-pressure phases of MgH_2 owing to the small energy differences involved and the (partly) reconstructive phase transitions. Such stabilization of MgH_2 high-pressure phases at room temperature would reduce the required storage space, volume of hydrogen, and in the extreme case the expected volume benefit would be ca. 19.5% for ϵ - MgH_2 compared with α - MgH_2 . The possibility of stabilizing the high-pressure modifications by chemical means would also be interesting to explore.

We have recently investigated pressure-induced structural transition in a series of aluminum hydrides with the composition $X\text{AlH}_4$ ($X = \text{alkali metals}$) which also have a high relative weight of stored hydrogen (7.5 and 10.6 wt.%, respectively, for NaAlH_4 and LiAlH_4). There should occur several pressure-induced structural transitions in this class of materials with large volume reduction at the phase-transition points and with small energy differences between the ambient- and high-pressure phases [34]. Hence efficient hydrogen-storage

materials with high volume density of hydrogen would be obtained if one could stabilize such high-pressure phases by chemical means.

2.3. Elastic properties

Structural intermetallics for high-temperature applications are currently in the center of interest owing to their high strength, oxidation resistance, high melting point, and for some of them also low density and high resistance against fatigue, wear, erosion, and cavitation. The hindrance to use these materials for structural applications is their brittleness especially at and below room temperature. World-wide development efforts have been focused on improving the ductility of structural intermetallics. As the elastic constants are the fundamental quantities for describing the mechanical properties of materials, it is of interest to estimate such quantities.

Elastic constants for most pure metals are available in the literature. In contrast, available data for technologically important alloys and intermetallic phases are very limited. In particular, single-crystal elastic constants are available only for a few intermetallic phases [35] partly owing to the difficulties involved in growing single crystals of sufficient size and also to estimate the parameters from experimental resonance spectra. Hence, efforts have been made to derive the elastic constants from first-principles DFT calculations. Although, the bulk modulus have been calculated for various materials, the calculations of the other elastic constants are relatively scarce. Even though many attempts have been made to calculate the elastic constants of cubic materials from first principles, very few attempts have been made to calculate the elastic constants for moderately low-symmetric cases such as tetragonal and hexagonal systems. The task of calculating the elastic constants for low-symmetric structures becomes more difficult when realizing that the strains needed in the calculation of some of them give rise to a geometry with very low symmetry. It has been recently demonstrated [36] that full-potential DFT calculation along with the GGA gives reliable prediction of elastic constants for low-symmetric materials such as orthorhombic TiSi_2 . Here we show the reliability of DFT calculations to predict elastic properties for the aerospace engineering material hexagonal Ti_3Al .

The hexagonal lattice is described by the parameters a and c with Bravais lattice vectors in matrix form:

$$\mathbf{R} = \begin{pmatrix} \frac{\sqrt{3}}{2} & -\frac{1}{2} & 0 \\ 0 & 1 & 0 \\ 0 & 0 & \frac{c}{a} \end{pmatrix}.$$

The VASP [37] method allows total-energy calculations to be performed for arbitrary crystal symmetry. One can

therefore apply small strains to the equilibrium lattice, determine the resulting change in the total energy, and from this information deduce the elastic constants. Linear combinations of the elastic constants can be determined by straining the lattice vectors \mathbf{R} by means of the matrix product $\mathbf{R}' = \mathbf{R} \cdot \mathbf{D}$, where \mathbf{R}' is a matrix containing the components of the distorted lattice vectors and \mathbf{D} is the symmetric distortion matrix, which contains the strain components. One must consider only small lattice distortions in order to remain within the elastic limit of the crystal. There are several distortions which can be used to determine the elastic constants. For several purposes it is convenient to consider volume-conserving or symmetry-preserving distortions. The internal energy of a crystal under a strain δ can be expanded in powers of the strain tensor with respect to the initial internal energy of the unstrained crystal. The energy of the strained lattice can be expressed by means of the second-power terms in a Taylor expansion with the distortion parameters δ as variables

$$E(V, \delta) = E(V_0, 0) + V_0 \left(\sum_i \tau_i \xi_i \delta_i + 1/2 \sum_{ij} c_{ij} \delta_i \xi_i \delta_j \xi_j \right) + O(\delta^3) + \dots \quad (1)$$

The volume of the unstrained system is denoted V_0 , $E(V_0, 0)$ is the corresponding total energy, τ_i an element of the stress tensor, and c_{ij} the elastic constants. With the five independent elastic constants for the hexagonal crystal systems one needs five different strains to determine them (see Ref. [38]). The total energies for the various distortions are calculated using the PAW implementation of VASP [37] with a sufficiently large number of \mathbf{k} points.

The calculated single-crystal elastic constants for Ti_3Al are compared with the experimental values [39] in Table 3. The theoretical data are obtained according to four different approaches such as local density approximation (LDA) [40] with and without relaxation of atom positions, and the GGA [41] with and without relaxation of atom positions. Most of the elastic constant calculations reported in the literature are obtained without the relaxation of atom positions due to the extensive computations involved in such calculations. If one does not take into account the atomic relaxation during the estimation of the total energy with distortion, one generally obtains higher values for the elastic constants (particularly the shear modulus) than found when atomic relaxation is included. Table 3 shows that the calculated elastic constants are closer to the experimental values when atomic relaxations are included. The calculated equilibrium volumes deviate from the experimental values by 3% and 8% according to our GGA and LDA calculations, respectively, and the single-crystal elastic constants obtained from GGA calculations are closer to the experimental values than

from LDA calculations. The bulk modulus from GGA calculations deviates only 4% from experiment compared with the 18% deviation found according to LDA calculations.

Fig. 6 depicts the anisotropy in the mechanical properties of Ti_3Al for the directional-dependent bulk modulus, Young's modulus, and shear modulus in planes parallel (ab plane) and perpendicular (ac plane) to the basal plane obtained [38] using the single-crystal elastic constants from experiment [39] and GGA and LDA from calculations. The bulk modulus obtained from the GGA calculations are found to be in excellent agreement with the experimental data in directions within the ab and ac planes. For the Young's modulus also the GGA calculations are in excellent agreement with the experiment within the ab plane, but show larger anisotropy in the ac plane than the experimental findings. The directional-dependent shear modulus in the ab plane obtained from LDA and GGA calculations are in good agreement with the experiment, but once again the theory shows larger anisotropy in the ac plane

than the experiment. The ratio of the linear bulk modulus along a and c are only 1.13 according to the GGA calculations. The mechanical anisotropy in Ti_3Al is not very large and this may be due to dominant metallic Ti–Ti bonding compared with the limited influence of the directional Ti–Al bonds.

2.4. Electronic structure and magnetism in transition-metal oxides

In recent years the number of experimental as well as theoretical studies on $3d$ transition-metal perovskite oxides (ABO_3 -type; A = rare-earth or alkaline-earth metals, B = transition metal) have increased following the discovery of high- T_c superconductivity in cuprates [42] and colossal negative magneto-resistance in manganites [43]. The electronic structure of perovskite-like transition-metal oxides are described by three crucial energy parameters: band width (W), Coulomb repulsive energy (U), and strength of the ligand field (Dq). Depending on the transition-metal atom, perovskites

Table 3
Experimental [39] and calculated single-crystal elastic constants (c_{ij}), bulk modulus (B) and shear modulus (G) for hexagonal Ti_3Al

Method	c_{11}	c_{12}	c_{13}	c_{33}	c_{44}	B	G
Exp.	1.83	0.891	0.626	2.25	0.641	1.062	0.528
GGA	1.872	0.914	0.706	2.261	0.528	1.105	0.482
LDA	2.097	1.042	0.818	2.553	0.509	1.253	0.500
GGA ^a	2.141	0.649	0.704	2.265	0.675	1.106	0.646
LDA ^a	2.385	0.753	0.818	2.553	0.724	1.253	0.700

All values are in Mbar.

^aWithout relaxation of atoms.

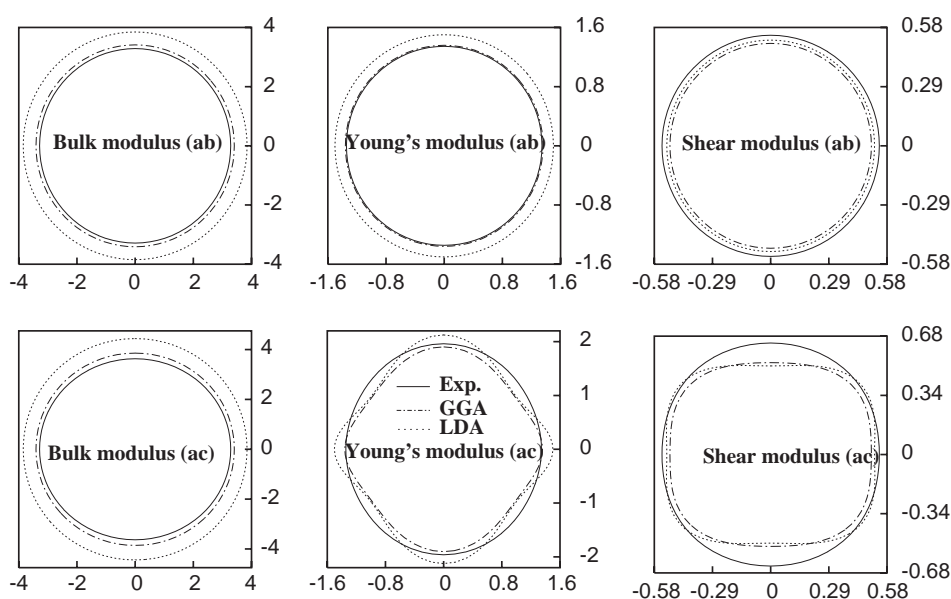


Fig. 6. Directional-dependent bulk modulus, Young's modulus, and shear modulus (values in Mbar) for hexagonal Ti_3Al obtained from single-crystal elastic constants according to experiment (Ref. [39]), GGA and LDA calculations in ab and ac planes.

exhibit either localized or collective behavior of the d electrons. Also depending upon the valence of the A -site cation, the valence of B changes and this leads to unusual magnetic and electronic properties. The simultaneous presence of strong electron–electron interaction within the $B-3d$ manifold and a sizable hopping–interaction tendency between the $B-3d$ and $O-2p$ states are primarily responsible for a wide range of properties exhibited by such compounds. Often the presence of a strong intra-atomic Coulomb interaction makes a single-particle description of such systems inadequate. Due to this deficiency, the traditional DFT calculations has often failed to predict the insulating behavior [44,45]. To overcome this deficiency of the local spin-density approximation (LSDA) to give the correct insulating properties of the perovskites, LSDA + U theory [46,47] is applied, where U is the intra-site Coulomb repulsion.

Transition-metal oxides are believed to be strongly correlated materials and hence the DFT often failed to predict the correct ground states for such systems. Some of the features lacking in most of the theoretical studies on ABO_3 -type perovskite-like compounds originate from the use of the atomic-sphere approximation (ASA), i.e., the calculations have not included the non-spherical part of the potential and also used a minimal basis set. Further the cubic perovskite structure is frequently assumed [44,48] and the importance of structural distortions are not taken into account. Moreover, owing to the presence of magnetic ordering, relativistic effects such as spin–orbit (SO) coupling may be of significance in these materials, but SO has been neglected in most of the earlier studies. Furthermore, it is shown that instead of using the uniform electron-gas limit for exchange and correlations (corresponding to LSDA) one can improve the outcome by including inhomogeneity effects through the GGA [49]. Hence, we used a generalized-gradient-corrected, relativistic full-potential method (GGCRFLMTO) with the experimentally observed distorted perovskite structure and proper magnetic ordering as the input in the calculations.

LaMnO_3 , LaFeO_3 , and LaCrO_3 stabilize in the orthorhombic GdFeO_3 -type structure. It can be viewed as a highly distorted cubic perovskite-type structure with a quadrupled unit cell ($a_p\sqrt{2}$, $a_p\sqrt{2}$, $2a_p$ where a_p is the lattice parameter of the cubic aristotype structure). The electronic configuration of Mn^{3+} in LaMnO_3 is postulated as $t_{2g}^3 e_g^1$ and, hence, a typical Jahn–Teller (JT) system. Basically, two different types of distortions are included in the crystal structure of LaMnO_3 . One is a tilting of the MnO_6 octahedra around the cubic [110] axis (as in LaFeO_3 and LaCrO_3) which leads to a change in the Mn–O–Mn angle from 180° to $\sim 160^\circ$. This is not directly related to the JT effect, but is attributed to the relative sizes of the components, say, expressed in terms of the tolerance factor $t_p = (R_{\text{La}} + R_{\text{O}})/\sqrt{2}(R_{\text{Mn}} + R_{\text{O}})$,

where R_{La} , R_{Mn} , and R_{O} are the ionic radius for La, Mn, and O, respectively, amounting to $t_p = 0.947$ for LaMnO_3 . The rotation of the MnO_6 octahedra facilitates a more efficient space filling. The second type of crystal distortion in LaMnO_3 is the deformation of the MnO_6 octahedra caused by the JT effect, viz. originating from the orbital degeneracy. This may be looked upon as a co-operative shifting of the oxygens within the ab plane away from one of its two nearest neighboring Mn atoms toward the others, thus creating long and short Mn–O bond lengths (modified from 1.97 Å in the cubic case to 1.91, 1.96, and 2.18 Å for the orthorhombic variant) perpendicularly arranged with respect to the Mn atoms. The long bonds can be regarded as rotated 90° within ab on going from one Mn to the neighboring Mn [50].

First we discuss the electronic structure and magnetic properties of LaMnO_3 . When ABO_3 compounds are in the antiferromagnetic (AF) state there are three possible magnetic arrangements according to inter- and intraplane couplings within (001). (i) With interplane AF coupling and intraplane ferromagnetic (F) coupling the A -AF structure arises. (ii) The opposite structure of A -AF, where the interplane coupling is F and the intraplane coupling is AF is called C -AF. In the C -type cell all atoms have two F and four AF nearest neighbors whereas the reverse is true for A -type AF. (iii) If both the inter- and intraplane couplings are AF the G -AF structure should arise [48]. In the G -type AF lattice, each Mn atom is surrounded by six Mn neighbors whose spins are antiparallel to those of the chosen central atom. Among the several possible magnetic orderings, the experimental studies show that for LaMnO_3 the A -AF ordering is the ground state with a Néel temperature (T_N) of 140 K.

In order to understand the role of structural distortion on the electronic structure and magnetic properties of LaMnO_3 total energies have been calculated for the experimentally observed orthorhombic structure and the hypothetical cubic structure in paramagnetic (P), F, A -AF, C -AF, and G -AF magnetic states. Consistent with experimental findings our calculations show that the ground state for A -AF LaMnO_3 is a semiconductor with an indirect gap of 0.278 eV (see A -AF LaMnO_3 in Fig. 7). DFT calculations also show strong couplings between lattice distortions, magnetic order, and electronic properties of LaMnO_3 . In particular, it is found that without the lattice distortions LaMnO_3 would have an F metallic ground state, and even if forced to be A -AF, it would still be metallic [51]. The F phase of LaMnO_3 is found to be just 24.7 meV above the ground state and has half-metallic character. We found a huge energy gain of 0.323 eV/f.u. for F and 0.407 eV/f.u. for A -AF when the structural distortions were included. Further, the cubic phase of LaMnO_3 is predicted to be in the half-metallic F state.

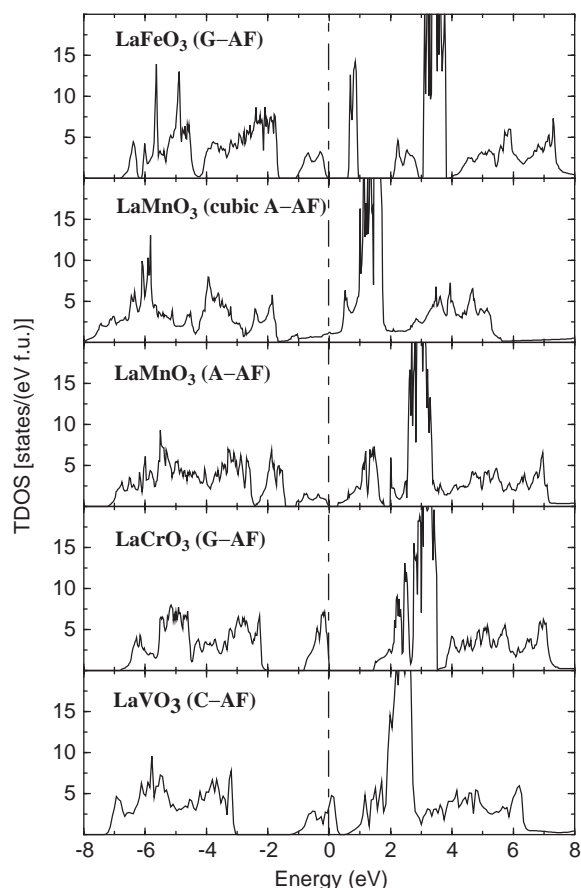


Fig. 7. Calculated total DOS for LaBO_3 ($B = \text{V, Cr, Mn, Fe}$) in the magnetic ground states obtained from gradient-corrected SO-coupling-included full-potential LMTO method. For $B = \text{Mn}$ also including the DOS for a hypothetical cubic perovskite aristotype structure with A -AF ordering.

The calculated total DOS for A -AF LaMnO_3 in the cubic as well as the experimentally found orthorhombic structure are given in Fig. 7. From this figure it is clear that the semiconducting behavior appears only when the structural distortions are included in the calculation whereas the cubic A -AF phase is predicted to be a metal. Further, even if we include the structural distortions in the calculations the P, F, and C-AF phases of LaMnO_3 exhibit metallic character. The JT distortion lifts the degeneracy of the e_g level. The e_g -level splitting is found to be 0.278 eV according to the calculation and this is nothing but the (semiconducting) band gap in this material. Saitoh et al. [52] reported strong covalency and suggested that the energy gap in LaMnO_3 should be considered as of the charge-transfer (CT) type. The band gap estimated from the DOS for A -AF state LaMnO_3 is found to be in good agreement with the value (0.24 eV) obtained by Mahendiran et al. [53] from resistivity measurements (Jonker [54] reported 0.15 eV). However, our value for the direct gap (0.677 eV) between occupied and empty states at the same location in the Brillouin zone (BZ) is too low compared with optical (1.1 eV) [55]

and photoemission (1.7 eV) [52] measurements. (However, it should be noted that experimental optical gaps are usually defined at the onset of an increase in spectral intensity in the measured optical variable.) It is also useful to compare our calculated band gap with other theoretical results. The LSDA and LSDA + U calculations of Yang et al. [56] using the LMTO-ASA method gave a band gap of 0.1 and 1.0 eV, respectively. The LSDA + U_2 approach (where U is applied only to the t_{2g} electrons) [57] yielded a band gap of 0.2 eV. Hence, our band gap is somewhat larger than that of other LSDA calculations. On the other hand, Hartree–Fock calculations [58] gave an unphysically large gap (3 eV) for LaMnO_3 .

Usually, the e_g splitting caused by the JT effect is somewhat underestimated in ASA calculations [44,45,57,59] and a discrepancy could reflect an uncertainty introduced by the ASA approach. It is worth to recall that when we performed a band-structure calculation for monoclinic SnI_2 with the widely used TBLMTO-ASA method [17] we found a band-gap of 0.72 eV only, whereas a value of 1.54 eV was obtained from the full-potential LMTO method without SO coupling [60]. These values are smaller than the experimental values by Kostyshin et al. [61] (2.52 eV at 85 K), Gorban et al. [62] (2.2 eV at 86 K), and Fujita et al. [63] (2.275 eV at 298 K). Hence discrepancies in band-gap values not only rise from the LSDA treatment, but also from other approximations used in the calculations. Even though our calculation predicts [64] the correct non-magnetic ground state for LaCoO_3 it failed to predict the semiconducting behavior (instead, E_F is lying on a pseudogap-like feature). It is interesting to note that optical conductivity studies [65] show a spin-gap energy of ~ 30 meV and a charge-gap of ~ 0.1 eV for this material. So the failure to obtain proper semiconducting behavior may be due to a small value for the charge gap, which is within the accuracy of the present type of calculations. The calculated band gap is here identified with the difference between the highest occupied and the lowest unoccupied Kohn–Sham eigenvalues, the so-called Kohn–Sham gap. The real band gap, however, is the smallest energy required to move an electron from the VB of the insulating N -particle ground state to infinity minus the energy gained by adding an electron to the conduction band (CB) of the insulating N -particle ground state. This gap can be written as a sum of the Kohn–Sham gap and a part originating from the discontinuity in the exchange-correlation potential at the integer particle number N [66]. Because of difficulties with the discontinuity, there are no standard methods for calculating (correctly) the size of band gaps, although recent work based on the GW approximation (where G is the Green function of a free electron and W is the screened interaction potential) seems promising in this regard [67]. These aspects are

not explored further in this review. The important conclusion arrived from the above observations is that in order to obtain reasonable band-gap values for semiconductors or insulators one has to include proper structural distortions and magnetic ordering in addition to the full-potential treatment.

As mentioned earlier, the JT distortion as well as the rotation of the octahedra are present in LaMnO_3 . In order to gain insight into the role of JT distortion and rotation of the octahedra we have carried out two sets of calculations for LaMnO_3 in the five different magnetic states (P, F, *A*-, *C*-, and *G*-AF). In one set we have taken into account only the JT distortion and neglected the rotation of the octahedra and in the other set vice versa. The first set of calculations gave *A*-AF as the ground state with 5.8 meV/f.u. lower energy than the second best choice, the F phase. In the other set with the opposite situation: we found that the F state is the ground state with 53.4 meV/f.u. lower energy than the *A*-AF phase. These results indicate that the lifting of the degeneracy in the band structures by JT distortion plays an important role in stabilizing the *A*-AF ordering in LaMnO_3 . Further, we found that both the rotation of the octahedra and the JT distortion are necessary to obtain the insulating behavior for LaMnO_3 . The energy separation between the e_g and t_{2g} levels, caused by the crystal-field splitting, is known to be larger than 1 eV [68]. Owing to strong overlap between the e_g and t_{2g} levels in the *A*-AF orthorhombic phase, we are unable to estimate the crystal-field splitting energy. However, owing to the well separated e_g and t_{2g} levels in the cubic phase we estimated this energy to be ~ 0.96 eV. The Mn d -exchange splitting obtained from our calculation is 3.34 eV in agreement with 3.5 eV found by Pickett and Singh [69] by linear-augmented plane-wave (LAPW) calculations and 3.48 eV reported by Mahadevan et al. [70] from LMTO-ASA calculations.

The orthorhombic LaFeO_3 is found to take an insulating *G*-AF-type arrangement with $T_N = 738$ K. We have calculated the total energies for P, F, *A*-, *C*-, and *G*-AF phases of LaFeO_3 using the GGCRFLMTO method. These correctly provide *G*-AF as the ground state for LaFeO_3 with *A*-, *C*-AF, F, and P phases higher in energy by 191, 132, 185, and 798 meV/f.u., respectively. Fig. 7 also show that LaFeO_3 in the *G*-AF phase is an insulator with a band gap of 0.61 eV. The observation of insulating behavior is in agreement with the experimental observation of a CT gap (2.1 eV according to optical measurements [55]). The calculated magnetic moment at the Fe site is $3.67 \mu_B$ which is comparable with $4.6 \pm 0.2 \mu_B$ obtained by neutron diffraction [71]. LaCrO_3 is also a CT insulator in the orthorhombic GdFeO_3 -type structure and has *G*-AF ordering with $T_N = 289$ K as the ground state. The calculated magnetic moment at the Cr site is $2.50 \mu_B$ which is in good agreement with $2.8 \pm 0.2 \mu_B$ obtained

by neutron diffraction [71]. Also, our calculations were able to reproduce the correct insulating ground state with a band gap of 1.48 eV (see Fig. 7). Experimental optical reflectivity measurements [55] yielded a band gap of 3.4 eV in this compound (remember: the usual LDA or GGA underestimates band gaps). The GGCRFLMTO calculations appear to be able to provide the correct ground state for CT insulators.

Arima et al. [55] measured the optical gap of LaTiO_3 and LaVO_3 and concluded that they are Mott insulators. In LaVO_3 , the magnetic transition occurs at 143 K, and the ordered spin configuration is *C*-AF [72] This compound undergoes another phase transition, a first-order structural transition (orthorhombic to monoclinic) at 141 K [73]. The calculated magnetic moment at the V site in LaVO_3 according to GGCRFLMTO calculation is $1.51 \mu_B$ /f.u. in good agreement with the experimental value of $1.3 \mu_B$ obtained by neutron diffraction [72]. Our calculations also correctly provide the *C*-AF phase as the magnetic ground state for LaVO_3 , while the *A*-, *G*-AF, F, and P phases are 20, 87, 25, and 310 meV/f.u. higher in energy, respectively. LaVO_3 is an insulator with an semiconducting gap [74] of about 0.2 eV and an optical gap of 1.1 eV [55]. Even though our calculations give the correct magnetic ground state and magnetic moment at the V site, it failed to reproduce the experimentally established insulating behavior of LaVO_3 . From the Fig. 7 it is clear that LaVO_3 is a metal with a finite DOS of 39.98 states/Ry/f.u. at the E_F . Also for LaTiO_3 the GGCRFLMTO calculations failed to reproduce the insulating behavior. So, we conclude that the GGCRFLMTO approach is not sufficient to study the ground-state properties of Mott insulators although it is quite successful in predicting insulating behavior for other such materials. It was understood many years ago that this problem is connected with the inadequate description of many-body effects in DFT calculations of excitation spectra. In order to overcome this failure, there are several remedies such as Coulomb-correlation-corrected DFT (LDA + U approach) [46], *GW* approximation (*GWA*) [67], self-interaction corrected DFT (LDA + SIC) [75], time-dependent DFT [76], dynamical mean-field theory (LDA + DMFT) [77] etc.

2.5. Magnetic phase-diagram studies in ruthenates

Ever since unconventional superconductivity was observed in Sr_2RuO_4 [78], ruthenates have attracted much interest. Poorly metallic non-Fermi liquid-behaving SrRuO_3 is the only known F ($T_C = 160$ K) $4d$ transition-metal oxide [79,80]. CaRuO_3 is also metallic, but experimental and theoretical studies conclude contradictory regarding the nature of the magnetic ground state [e.g., AF [79,81,82], nearly F [83], exchange

enhanced paramagnetic [84], Curie–Weiss paramagnetic [85], verge of F instability [86], spin glass (SG) [87] etc.], and this controversy is not settled yet. CaRuO_3 and SrRuO_3 are isostructural and isoelectronic, differing structurally only in the degree of the small orthorhombic distortion (lattice constants within 2%). Hence, insight into the magnetic properties of these compounds is expected to increase the general knowledge on magnetic phenomena in perovskite oxides, and ruthenates in particular. The striking difference in the magnetic properties of SrRuO_3 and CaRuO_3 motivated us [88] to undertake magnetic phase-diagram studies on $\text{Sr}_{1-x}\text{Ca}_x\text{RuO}_3$.

We made a series of gradient-corrected relativistic full-potential DFT calculations [88,89] for Ca-substituted SrRuO_3 in P, F, and A-, C-, and G-type AF states. The calculated total energy for CaRuO_3 from GGA calculations with and without SO coupling for different magnetic configurations show that SO coupling appears to play an important role in deciding the magnetic properties of ruthenates.

The experimentally found spontaneous magnetic moment [83] and Weiss temperature [90] for $\text{Sr}_{1-x}\text{Ca}_x\text{RuO}_3$ are given in Fig. 8 along with the calculated total-energy difference relative to that of the F phase for the various magnetic configurations. An increase in x decreases the F interaction and increases the G-AF interaction. Because of the smaller ionic

radius of Ca compared with Sr (0.99 vs. 1.18 Å), tilting of the octahedra occurs when one substitutes Ca for Sr in SrRuO_3 which in turn affects the magnetic properties. Fig. 8 shows that the F to G-AF transition takes place around $x = 0.75$ both experimentally and theoretically. This confirms the presence of AF interactions in CaRuO_3 . However, neutron powder-diffraction diagrams at 8 K show [89] no sign of extra Bragg reflections, which should have been the proof of long-range AF ordering. Owing to the small total-energy differences between the AF and F phases of CaRuO_3 (see Fig. 8), there is likely to be a competition among the different AF and F interactions, in the sense that no single configuration of the moments is uniquely favored by all interactions (viz. frustration) and hence SG behavior may appear. Recent magnetization measurements [87] show distinctions between the zero-field-cooled and field-cooled characteristics which could confirm the presence of SG behavior with finite moments at the Ru sites.

2.6. Magnetic properties of lanthanides and actinides

The spin DFT is currently utilized as a tractable starting point for first-principle calculations of the electronic structure and magnetic properties of condensed-matter systems [66,91]. For applications to lanthanide and actinide metals and their alloys, a relativistic generalization to the spin DFT is needed. Treating the consequences of correlation effects on the magnetic behavior in the transitional regime (neither atomic like nor itinerant) of $4f$ or $5f$ localized situation is a central problem in condensed-matter science [92]. Localized character significantly affects the orbital magnetization, and the understanding of the magnetism requires mapping not only of total moments but of spin and orbital moments individually. The spin polarization and SO coupling account for the interactions and give rise to Hund's first and third rule for atoms. However, a good calculation of the orbital contribution to the total moment also requires that the interactions responsible for Hund's second rule are taken into account, viz. that the total orbital moment should be maximized at the maximum spin configuration. This effect has been included via an orbital-polarization (OP) term [93] into a band Hamiltonian. In general the degree of localization of $5f$ electrons in the actinide series lies between that of the $4f$ electrons in the lanthanide series and that of the $3d$ electrons in transition metals. It is assumed that the $4f$ and $5f$ electrons are itinerant and to explore this aspect we examined the nature of the electronic structure and magnetic properties of cerium and uranium monochalcogenides. The assumption that the $5f$ electrons are itinerant is most probably correct for the actinide compounds with smaller lattice parameters, but is not generally accepted for those with larger lattice

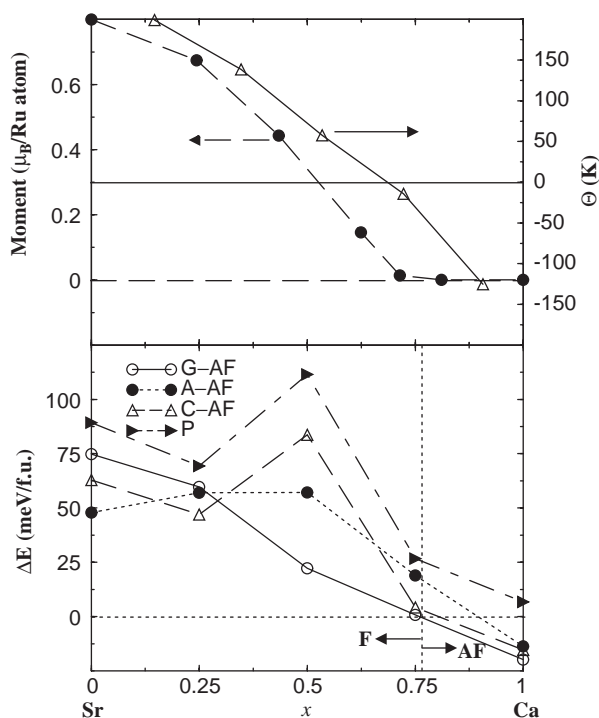


Fig. 8. Magnetic phase-diagram data for $\text{Sr}_{1-x}\text{Ca}_x\text{RuO}_3$. The upper panel shows the experimental spontaneous magnetic moment [83] and Weiss temperature [90]. The lower panel gives energies relative to the total energy for the F phase.

parameters such as UTe. Considering the change from US to UTe and CeS to CeTe, one can vary the $5f-5f$ and $4f-4f$ separation and hence the degree of localization. So, we studied the magnetic properties of uranium and cerium chalcogenides with the spin DFT at different levels of approximations.

In order to account for the magnetic properties of lanthanide and actinide compounds one has to calculate the orbital moments reliably. From analyses of experimental and theoretical magnetic anisotropy energy (MAE), Jansen [94] concluded that the energy functional together with the SO coupling must contain terms which depend directly on the orbital moment. Based on van Vleck and Racha's vector model for atomic multiplets an approximate energy expression for Hund's second rule is derived [93,95,96]. The OP energy for a particular spin-quantization direction \hat{n} was found to be well approximated by

$$E_{\text{OP}}^{\hat{n}} = -\frac{1}{2} \sum_{\sigma} B L_{z,\sigma}^{2\hat{n}}, \quad (2)$$

where B (for d states) is a Racah parameter [97] and $L_{z,\sigma}$ is the z component of the orbital-angular momentum of the spin state σ in the \hat{n} direction. Just as the spin moment can be written as the expectation value of s_z one can calculate the orbital moment. The orbital magnetic moment at the N th site is given by the expression [98]

$$\langle \hat{L}_z^{\hat{n}} \rangle_N = \frac{\mu_B}{(2\pi)^3 \Omega} \sum_i \int dk \langle ik | \hat{L}_z^{\hat{n}} | ik \rangle_N, \quad (3)$$

where i refers to a given occupied relativistic band state, the z projection of the orbital moment operator is \hat{L}_z ,

and Ω is the unit-cell volume. The expectation value $\langle ik | \hat{L}_z^{\hat{n}} | ik \rangle_N$ is calculated over the N^{th} atomic site.

The physical meaning of OP is that states with different angular momentum have different angular shape and hence different Coulombic interactions, which via Eq. (2) are included in the energy functional. Applying this energy expression to solids one finds that it gives rise to energy shifts for single-particle states with different magnetic quantum numbers. The OP term is included in the diagonal elements of the Hamiltonian matrix. Thus at each atom site, OP is taken into account by means of an eigenvalue shift, $\Delta V_{m_l} = -B L_z m_l$, which depends on the quantities obtained from the previous iteration step. The entire process is self-consistent and no other parameters were adjusted. This means that the calculations incorporate all three Hund's rules (spin splitting, orbital splitting, and SO splitting) and is within the stated approximations, fully self-consistent. The computed values of site-projected spin and orbital moments for cerium and uranium chalcogenides are collected in Table 4. Also given are the total magnetic moments obtained by summation of spin moments (including those from interstitial regions), orbital moment, and experimental values. First we look at the calculated magnetic moments for the cerium chalcogenides obtained at different levels of approximations. We observe large orbital moments at the Ce site. The induced spin and orbital moments on the chalcogenide atoms are antiparallel to those on the Ce atoms, and are very small. In the usual LDA + SO calculation we found that the spin moments are almost equal and antiparallel to the orbital moments resulting in almost zero net

Table 4

Site-projected spin and orbital moments and total moments (all in μ_B) for CeS, CeTe, US, and UTe (generally AX) in the F phase obtained from different approximations using the full-potential LMTO method

Compound	Method	A^{spin}	X^{spin}	$A^{\text{orb.}}$	X^{orb}	$AX^{\text{tot.}}$	Expt. tot.
CeS	LDA	-0.567	0.007	0.598	-0.003	-0.021	0.57 ± 0.03^a
	LDA + OP	-0.837	0.008	1.459	-0.006	0.554	
	GGA	-0.795	0.015	0.773	-0.004	-0.111	
	GGA + OP	-0.999	0.015	1.854	-0.009	0.731	
CeTe	LDA	-0.942	0.009	0.923	-0.002	-0.099	0.3 ± 0.1^b
	LDA + OP	-1.085	0.011	1.928	-0.004	0.754	
	GGA	-1.088	0.018	0.956	-0.002	-0.234	0.45 ± 0.20^c
	GGA + OP	-1.193	0.019	2.220	-0.004	0.920	
US	LDA	-1.542	0.000	1.980	-0.024	0.201	1.7 ± 0.03^d
	LDA + OP	-1.837	0.010	3.417	-0.025	1.357	
	GGA	-1.899	0.022	2.100	-0.023	-0.082	
	GGA + OP	-2.092	0.030	3.594	-0.024	1.251	
UTe	LDA	-2.189	0.019	2.978	-0.016	0.562	2.2 ± 0.1^d
	LDA + OP	-2.458	0.027	4.462	-0.011	1.818	
	GGA	-2.577	0.043	2.946	-0.015	0.091	
	GGA + OP	-2.740	0.046	4.650	-0.010	1.673	

^aNeutron diffraction [101] at 4.2 K.

^bNeutron diffraction [102] at 1.5 K.

^cMagnetization [102].

^dNeutron diffraction [99] at 4.2 K.

moments for both CeS and CeTe against the finite moments experimentally established.

Now we try to understand the origin of the antiparallel alignment of spin and orbital moments in these systems. Compounds of the light lanthanides (actinides) have less than half-filled $4f$ ($5f$) band, therefore the induced orbital moments are antiparallel to the $4f$ ($5f$) spin moments. The diffuse electron-spin moment “ spd ”, mostly from $5d$ states for the Ce compounds and $6d$ states for the U compounds, are observed to be antiparallel to the total moment. This inference is obtained by comparing the observed relative magnitudes of f -electron and total moments by neutron scattering and magnetization measurements [99,100]. Only if the orbital component of the moment at the lanthanide (actinide) site is larger than, and antiparallel to, the spin component can theory and experiment be consistent. In these cases the sign of the total moment is determined by the orbital component.

When we used the GGA we found that the spin moment at the Ce site increases and hence we get small total moments which are much smaller than the experimentally observed values (see Table 4). However, when we include OP correction (LDA + OP or GGA + OP) the orbital moment increases to almost the double, resulting in good agreement between theoretical and experimental total moments. So, the total moment in such systems are determined by the orbital contribution. For the uranium chalcogenides also we found a similar impact of the OP correction; such computational improvements are the condition for a correct account for the total moments. From magnetic Compton scattering experiments [103] the orbital moment from the $5f$ electrons of UTe is $3.48 \mu_B$ and comparable with the calculated value of $4.38 \mu_B$ according to LDA + OP.

Next we look at the variation of the magnetic moment on changing the chalcogenide component. Compared to S^{2-} (1.84 Å) the size of Te^{2-} (2.21 Å) [104] is large and consequently the Ce–Ce (U–U) distance increased from 4.094 Å (3.881 Å) to 4.498 Å (4.357 Å). Hence, the narrowing of the bands due to localization of the electrons tends to increase the size of both the spin and orbital moment on going from sulfides to tellurides. The GGA appears to improve the total magnetic moments compared with those according to the LDA in the case of cerium chalcogenides owing to the enhancement in orbital moments. However, in uranium chalcogenides such treatment worsens the calculated total moments (LDA gave finite total moments whereas those obtained from GGA were negligible). Hence, we are unable to see a consistent pattern in the calculated magnetic moments for both lanthanides and actinides by the inclusion of the gradient corrections. More systematic studies are needed to arrive at a correct conclusion.

2.7. Magnetic anisotropy energy

Ferromagnetic materials exhibit intrinsic “easy” and “hard” directions of magnetization. This magnetic anisotropy is, both from technological and fundamental points of view, among the most important properties of magnetic materials. Depending on the type of application, materials with high, medium, and low magnetic anisotropy will be required, e.g., for permanent magnets, information storage media, magnetic cores in transformers, and magnetic recording heads. Many potential applications of epitaxial ferromagnetic films on semiconductor substrates require a perpendicular component of the magnetization. Such a configuration would permit perpendicular magnetic recording or magneto-optical (MO) recording employing either the Faraday effect (in transmission) or the MO Kerr effect (MOKE; in reflection) to rotate the plane of polarization of light propagating perpendicular to the substrate. Magnetic layers with strong perpendicular magnetic anisotropy (PMA) are of great interest for MO recording media with predicted performances of up to 300 Gbit/inch², in comparison with present commercial hard disks which have storage densities around 2 Gbit/inch² [105]. As the mechanisms responsible for PMA are so poorly understood, the search for new materials currently proceeds empirically. Hence, it is important to investigate the microscopic origin of magnetic anisotropy in detail in order to identify potential candidates (see Ref. [106]).

Calculations based on a modified (needed to treat the MAE problem [107]) FPLMTO [108] method was used. Usually the calculated orbital moment for such systems from relativistic calculations are lower than the experimental values. Hence, the OP term is included in the diagonal elements of the Hamiltonian matrix. This correction has yielded larger orbital moments for Fe, Co, and Ni and thus a better agreement for the calculated g factors for Fe and Co with experiment [95]. The energy involved in rotating the magnetization from a direction of low energy toward one of high energy is a measure for the magnetic anisotropy. We define the magnetic anisotropy energy as the difference in total energy between the magnetization within the plane (i.e., $\hat{n} = [110]$) and along [001]. Hence, according to this definition positive MAE means that the easy axis is along c and the hard axis within the ab plane. The MAE obtained from the relativistic full-potential LMTO method with SO and with SO + OP calculations are given in Table 5 along with available experimental values.

It should be noted that for all phases the easy axis is correctly predicted, both with and without OP, but only fair agreement between the experimental and theoretical energies is obtained from the SO calculations. The MAE is roughly doubled (except for NiPt) when OP is

Table 5

Calculated magnetic anisotropy energies (MAE in meV) obtained from relativistic FPLMTO calculations without (only SO) and with OP corrections (SO + OP). The results are compared with experimental and other theoretical values. All cases with easy axis along [001]

Phase	SO	SO + OP	Theory (others)	Experiment
CoPt	1.052	1.642	1.50 [109]	1.451
		1.782 [110]		1.583 [111]
				1.665 [112]
				1.0 [113]
FePd	0.154	0.342	0.55	0.5204 [114]
				0.48 [115]
				0.63 [111]
				0.5898 [116]
				0.55 [113]
FePt	2.734	2.891	2.8 [109]	0.8811 [114]
		2.258 [110]		2.75 [113]
MnPt	4.696	5.342	—	—
NiPt ^a	1.248	0.239	—	—

^a Experimental easy axis is found [117] along [001].

included, which moves the calculated values closer to the experiment. The experimental MAE for Fe, Co, and Ni are of the order of $\mu\text{eV}/\text{atom}$ [118]. The examined binary layered materials have MAE of the order of meV/f.u. indicating that the magnetic anisotropy may be further enhanced by orders of magnitude in multi-component systems with properly selected constituents. In order to understand the role of exchange splitting and SO coupling on the MAE of these bilayer materials we show the magnetic moment vs. MAE and average SO coupling constant (ξ_{av}) vs. MAE in Fig. 9a and b, respectively.

A detailed analysis [106] indicates that large MAE in such bilayer materials originate from the combined effects of tetragonal structural distortion, exchange splitting, and SO splitting from (at least) one of the constituents.

2.8. Metamagnetism and spin-state transition

The magnetic properties of the cobaltites depend on the spin state of Co^{3+} and Co^{4+} , i.e., whether the ions are in the low-, intermediate- or high-spin state. LaCoO_3 itself is a nonmagnetic insulator at low temperature, usually referred to as a low-spin state (LS, $S = 0$) because the atomic configuration $t_{2g}^6 e_g^0$ of Co^{3+} has no magnetic moment. Magnetic susceptibility slowly increases with temperature and reaches a maximum at $T \approx 90$ K. Above this temperature, the system shows a Curie–Weiss law behavior, followed by another transition at 500 K. While it is generally agreed that the low-temperature phase is in a nonmagnetic LS state both high-spin [119–124] (HS, $S = 2$, $t_{2g}^4 e_g^2$) and intermediate-spin (IS, $S = 1$, $t_{2g}^5 e_g^1$) state [125,126] have been proposed for LaCoO_3 at higher temperature. It is also

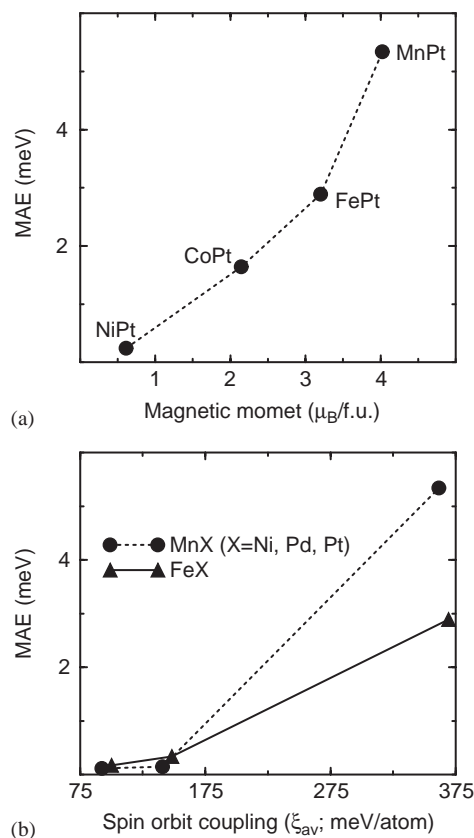


Fig. 9. Changes in magnetic anisotropy energy (MAE) for bilayer materials by variation of (a) magnetic moment and (b) average SO-coupling constant ξ_{av} .

suggested that the spin-state transition in LaCoO_3 occurs in two steps [122,127]. First, a conversion from the ground LS to IS state around 100 K. Second, a change from the IS state to a mixed IS-HS state around 500 K.

The attempts to explain the spin-state transition in LaCoO_3 based on different experimental techniques has resulted in a rather controversial picture. Direct magnetic measurements allow unambiguous identification of only the LS state below 50 K [65,120,126,128–131]. The behavior of the magnetic susceptibility in the region around 100 K has been interpreted in terms of thermal activation of a magnetic HS state from the LS ground state [120,128,132]. Abbate et al. [123] have interpreted the transition in the range 400–650 K as due to an LS-to-HS transition, based on X-ray absorption and X-ray photo-electron spectroscopy measurements. Saitoh et al. [126] have argued that the 100 K transition is most likely due to an LS-to-IS transition, and also suggested that the 500 K transition is due to the population of the HS state. Polarized neutron-scattering measurements [122] exhibit two magnetic-electronic transitions, one near 90 K and another near 500 K. The spin-state transition is maintained to occur at low

temperature, and the higher-temperature transition is not dominantly of magnetic origin. NMR [133] studies also claim that the LS-to-HS spin-state transition occurs at ~ 90 K. From temperature-dependent susceptibility and Knight-shift measurements [134] it has been pointed out that the LS-HS model is not applicable for understanding the spin-state transition in LaCoO_3 and thus an LS-IS model is more appropriate. Heikes et al. [119] considered an IS state to account for the effective moment obtained from susceptibility data below the ~ 500 K transition. From photoemission measurements it has been concluded that the hybridization of O-2*p* and Co-3*d* orbitals stabilize the IS state [135]. Heat-capacity measurements also support an LS-to-IS transition [136]. Recent magnetic susceptibility and neutron-diffraction studies [137] show that LaCoO_3 has the LS Co^{3+} configuration at the lowest temperatures. Below 350 K IS remains isolated and localized; and above 650 K all trivalent Co ions are claimed transformed to the IS state with itinerant *d* electrons. The main controversies are related to the nature of the transition, the temperature range of the transition, and to the electronic structure and hence to the energy levels involved. In order to gain a better understanding of the spin-state transition in LaCoO_3 and the origin of the P state with local magnetic moments, we have examined the energetics of various spin-ordered states as a function of hole doping and temperature.

Conventional spin-polarized calculations based on DFT allows the moment to float and the ground state is obtained by minimizing the energy functional with respect to the charge and magnetization densities, $[\rho(r)$ and $m(r)]$, under the constraint of a fixed number of electrons (N). In cases where two (or more) local minima occur for different moments, conventional spin-polarized calculations become difficult to converge or may “accidentally” converge to different solutions. Although LaCoO_3 is magnetically non-cooperative (hereafter “non-magnetic”) our conventional spin-polarized calculations always converged to a F solution with a moment of $1.2 \mu_B/\text{f.u.}$ In order to study spin fluctuations it is advantageous to calculate the total energy as a function of magnetic moment using the so-called fixed-spin-moment (FSM) method [138–140]. In this method one uses the magnetic moment (M) as an external parameter and calculates the total energy as a function of M . The condition of having a fixed-spin moment corresponds to using two different chemical potentials. With the variational principle this corresponds to minimizing the functional (F)

$$F[\rho(r), m(r)] = E[\rho(r), m(r)] - (\mu + h) \left[\int \rho^\uparrow(r) dr - N^\uparrow \right] - (\mu - h) \left[\int \rho^\downarrow(r) dr - N^\downarrow \right], \quad (4)$$

where μ is the chemical potential, h is the Lagrange multiplier which applies to the constraint of a fixed-spin moment $M = N^\uparrow - N^\downarrow$, and $\rho(r)$ and $m(r)$ are charge and spin densities, respectively [138].

Itinerant-electron metamagnets possess an anomalous temperature dependence of the susceptibility which increases with temperature and then decreases after a maximum at a finite temperature (T_m) and usually obeys the Curie–Weiss law at higher temperatures [141,142]. LaCoO_3 also shows a temperature-dependent magnetic susceptibility with an increasing trend at low temperature and a marked maximum around 90 K followed by a Curie–Weiss-law-like decrease at higher temperatures [122,130] which is similar to that of the itinerant metamagnets. The energy needed to enforce a given magnetic moment is given by the total-energy difference ΔE with respect to the “non-magnetic” case. The ΔE vs. magnetic-moment curve is shown in Fig. 10a for LaCoO_3 at 4 K. At low temperature, the ground state of LaCoO_3 corresponds to the non-magnetic LS state. However, the minimum of the F IS state occurs about 32 meV above the LS state (Fig. 10a). The existence of

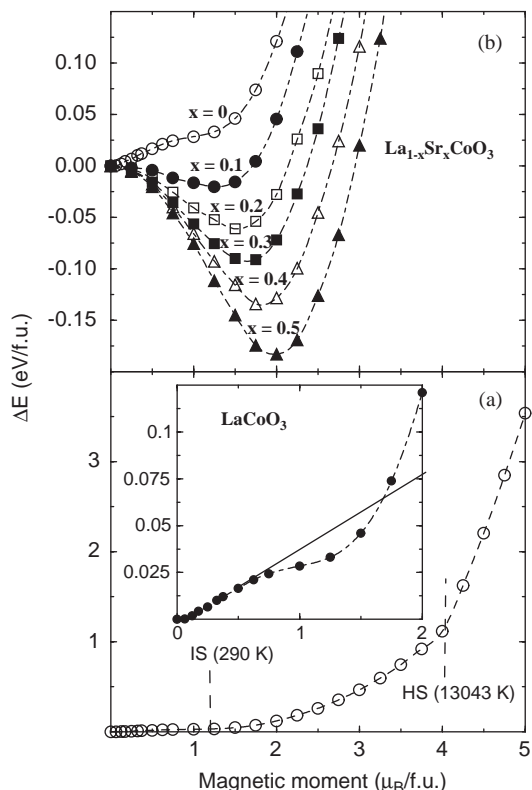


Fig. 10. (a) Total energy of LaCoO_3 as a function of constrained spin moment obtained for volume corresponding to 4 K. The zero level is chosen at the “non-magnetic” energy minimum. The inset gives an enlargement for the energy interval close to IS. The extrapolation of the metastable state above 25 meV is indicated by the straight line. Vertical dashed lines represent the cross-over to IS and HS and the corresponding temperatures required to excite the system to these states. (b) FSM curves for $\text{La}_{1-x}\text{Sr}_x\text{CoO}_3$ ($x=0-0.5$) obtained by FLAPW VCA calculation.

a F solution as a quasi-stable state implies that a discontinuous transition in magnetization would be possible by application of a magnetic field. The applied external field shifts the up- and down-spin bands by a small amount. As a consequence the system gains potential energy owing to the reduced Coulomb interaction, but at the same time loses energy owing to an increase in the kinetic energy. The final induced magnetic moment will be given by the balance between these two terms. However, in some systems there will, for a certain critical value of the applied field, occur a sudden gain in potential energy which is not sufficiently counterbalanced by the kinetic term. Hence, a metamagnetic spin state develops [143].

A detailed examination of the energy vs. moment shows a flattened region in the vicinity of $1.2 \mu_B$ (inset to Fig. 10a) where the F state gets stabilized according to the F spin-polarized calculations. So, it seems appropriate to assign a moment of $1.2 \mu_B$ to the IS state. The DOSs for the IS and HS states show that non-bonding t_{2g} electrons are present at E_F in the minority-spin state. Consequently these states are at an energetically higher level than the LS state (Fig. 10a). The energy difference between the LS and HS states of Co^{3+} ions is reported [119] to be less than 80 meV and may even be as low as 30 meV [65]. From magnetization measurements the energy difference between the LS and HS states is reported to be 6–22 meV [121,144,145]. Asai et al. [131] estimated the energy of the IS and HS states at 0 K to be 22.5 and 124.6 meV above LS, respectively. The calculated energy differences (see Fig. 10a) between the LS and IS states is 32 meV and that between LS and HS states 1113 meV. As the HS state is much higher in energy than the LS and IS states, the possibility of stabilizing the HS state by temperature and/or hole doping is not very favorable in a system like $\text{La}_{1-x}\text{Sr}_x\text{CoO}_3$. Hence, the present calculations rule out the possibility of stabilizing mixed-spin states such as LS-HS and IS-HS. Since Co^{3+} is a d^6 case, LS would be more stable than HS if the crystal-field splitting of the $3d$ states into t_{2g} and e_g levels is larger than the intra-atomic exchange splitting (i.e., $10Dq > 2J$). Conversely, if the exchange energy dominates, the result would be an HS state with $S = 2$. Owing to the degenerate nature of the IS state with $S = 1$, it is not possible to obtain stabilization within this framework. However, if hybridization with the oxygen band is taken into account the stability of an IS situation can be accounted for. In Fig. 10a, nearly degeneracy of the LS and IS states occurs because the intra-atomic exchange splitting Δ_{ex} of the $S = 1$ state is close to the crystal-field splitting Δ_{cf} .

It has been reported [146–148] that the $\text{La}_{1-x}\text{Sr}_x\text{CoO}_3$ phase develops F long-range order above $x = 0.05$ and that the metal–insulator transition takes place at $x \approx 0.2$. Optical measurements [149] show that the electronic structure of the high-temperature metallic state of

LaCoO_3 is very similar to that of the doping-induced metallic state. Hence, the FSM calculations on hole-doped LaCoO_3 is expected to give a better understanding about the nature of the temperature-induced spin-state transition. From the FSM curve obtained as a function of x (Fig. 10b), it is clear that the LS phase of Co^{3+} is the most stable among the magnetic configurations for $x = 0$, but the LS state is found to be unstable with increasing values of x . The instability of the “non-magnetic” phase on hole doping is consistent with the experimentally observed P behavior of the susceptibility for $x \geq 0.08$ [122]. The total DOS for LaCoO_3 in the LS state shows [138] that E_F is located in a deep valley, viz. being in a “non-magnetic” state. The hole doping shifts E_F to the peak on the lower energy side of DOS. As a result the Stoner criterion for band ferromagnetism becomes fulfilled and co-operative magnetism appears. The equilibrium spin moment for $\text{La}_{1-x}\text{Sr}_x\text{CoO}_3$ as a function of x , calculated according to FSM-VCA is found to be in excellent agreement with the experimental findings [150,151] as well as previous FPLMTO results [64]. This indicates that the FSM method is reliable to give correct predictions for equilibrium magnetic phases. The disappearance of the metamagnetic behavior and the appearance of the F state on hole doping of LaCoO_3 can be understood as follows. The reduction in the number of valence electrons by the Sr substitution shifts E_F to the lower energy side of VB toward the peak position in the DOS. As a result, the Stoner criterion becomes fulfilled and the metastable state becomes stabilized.

Calculations of the electronic structure for LaCoO_3 with lattice parameters for 1248 K can imitate the influence of the temperature via thermal expansion. The HS state (with $4 \mu_B$) lies much higher in energy than LS and IS at low as well as high temperature indicating that it is less probable to stabilize the HS state by temperature/hole doping. However, the FSM calculations show that the IS state is always lower in energy than the HS state for hole-doped LaCoO_3 . So, theory rules out the possibility of stabilizing HS or mixed spin states by either temperature or hole doping. Hence, the LS-to-IS spin-state transition is the more probable transition in LaCoO_3 . In conformity with this view point the calculated X-ray emission spectrum (XES) for LaCoO_3 in the LS and IS states are in good agreement with the experimental spectra measured at 85 and 300 K, respectively [152].

2.9. Spin, charge, and orbital ordering in perovskite-like oxides

In reduced band-width systems, such as $3d$ transition-metal oxides, the close interplay between spin, charge, and orbital is quite important to understand many unconventional physical properties and has been the

subject of extensive research in recent years [153–155]. There is a strong coupling between the crystal structure, magnetic order, and electronic properties. Understanding of the spin-, charge-, and orbital-ordering processes, and the interactions among them, provides a foundation for a deeper penetration into the complex behaviors of CMR materials. The CMR phenomena in perovskite-like manganites, on application of an external magnetic field tends to realign localized AF-arranged t_{2g} spins ferromagnetically. The transfer integral (t) of the e_g electron thus increases due to the strong Hund's-rule coupling between the t_{2g} and e_g electrons. Moreover, the application of the magnetic field promotes a transition from an insulating AF charge- and/or orbital-ordered state to an F metallic state accompanying a resistivity change by several orders of magnitude. The t of the e_g electrons between neighboring Mn sites in LaMnO_3 is mediated by the O-2p state and hence dependent on the degree of hybridization between the Mn-3d and O-2p orbitals. The Mn^{3+} ions in LaMnO_3 possess the electronic configuration $3d^4; t_{2g}^3 e_g^1$ with JT distortion due to ordering of e_g electrons which lead to A-AF insulating behavior [51]. Therefore, t is sensitive to the orbital ordering (OO) and this will play an important role for the physical properties. Reduction in the hybridization interaction (e.g., due to the tilting of the MnO_6 octahedra by lattice mismatch and JT distortion) causes narrowing of the W of the e_g band and tends to destabilize the double-exchange-mediated F state owing to the presence of competing instabilities, such as AF-superexchange interaction between the localized t_{2g} spins, charge ordering (CO) and/or OO, and JT-type electron-lattice coupling [156,157].

Our interest in looking at spin dynamics of the CMR manganese oxides is largely directed to the solution of the heuristic relation between electron correlations and magnetic interactions, or the possible mechanism for how quantum spins and orbitals are involved in the electron motions in the anomalous metallic state of these oxides. The ordered oxygen-deficient double-perovskites $\text{REBaT}_2\text{O}_{5+\delta}$ (notably $T = \text{Mn, Fe, and Co}$) have

attracted much attention as new spin-charge-orbital coupled CMR materials. The prototypical spin, charge, and orbital ordering in perovskite-like materials can be illustrated by taking as an example the oxygen-deficient double-perovskite YBaMn_2O_5 [158].

Recently Millange et al. [159] have succeeded in preparing phase-pure YBaMn_2O_5 and these authors reported crystal and magnetic structure parameters according to space group $P4/nmm$: $a = 5.5359 \text{ \AA}$, $c = 7.6151 \text{ \AA}$; Y in 2(b), Ba in 2(a), Mn(1) in 2(c) with $z = 0.2745$, Mn(2) in 2(c) with $z = 0.7457$, O(1) in 8(j) with $x = 0.4911$, $y = 0.9911$, $z = 0.4911$, and O(2) in 2(c) with $z = 0.0061$. The lacking oxygens in the yttrium plane, compared with the perovskite-prototype structure reduce the coordination number of yttrium to 8, while barium retains the typical 12 coordination of the perovskite structure. The Mn–O network consists of double layers of MnO_5 square pyramids, corner shared in the ab plane and linked *via* their apices. As seen from Fig. 11a the two kinds of MnO_5 pyramids are arranged in an ordered manner, each Mn^{2+}O_5 pyramid being linked to five Mn^{3+}O_5 pyramids and vice versa. Owing to this CO, each Mn^{2+} has four Mn^{3+} in-plane neighbors. Oxygen takes two crystallographically different sites: O(1) forms the base of the square pyramids, while O(2) is located at the apices of the pyramids. The interatomic Mn–O distances fall in four categories, 1.908 and 2.086 \AA for $\text{Mn}^{3+}\text{--O}(1)$ and $\text{Mn}^{2+}\text{--O}(1)$, respectively, whereas O(2) is 2.081 and 1.961 \AA away from Mn^{3+} and Mn^{2+} , respectively.

2.9.1. Spin ordering

All spin–spin interactions that form the basis for long-range magnetic ordering largely depend on the interplay between Coulomb energies and the Pauli-exclusion principle. Hund's rule emerges from the fact that electrons of parallel spin are forced by the Pauli-exclusion principle to occupy different orbital arrangements at each single atom as well as by the interacting electrons of neighboring atoms [160]. In manganites perovskites, the super-exchange AF interaction is

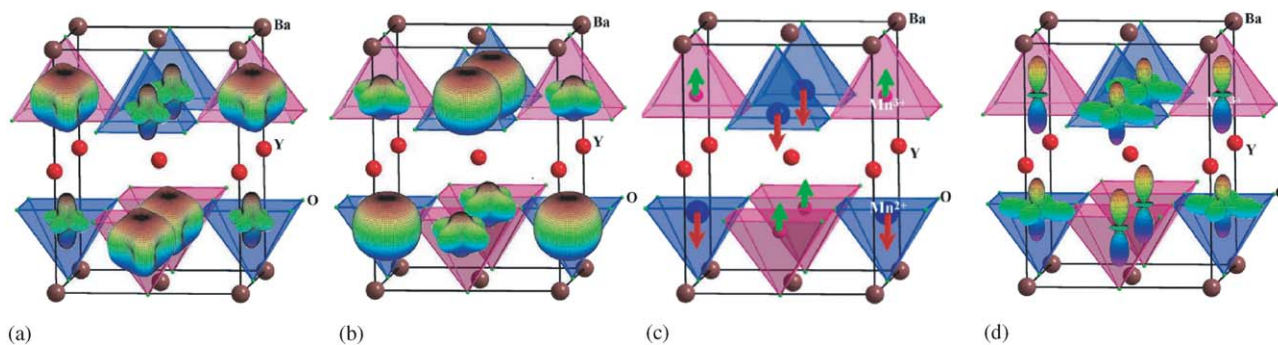


Fig. 11. Calculated Mn d -electrons density distribution for (a) up-spin and (b) down-spin electrons, (c) G-type Ferri spin ordering in YBaMn_2O_5 , and (d) the valence-electron distribution within 1 eV from E_F in the VB. The Mn ions in blue-colored square pyramids have oxidation state 2+ and those in majenda-colored square pyramids have 3+ state.

involved through a virtual electron transfer between half-filled t_{2g} orbitals which is constrained by the Pauli-exclusion principle to have a component of the transferred electron-spin antiparallel to those of the acceptor atom (e.g., *G*-AF LaCrO₃). On the other hand the double-exchange interaction involves a real electron transfer from a filled e_g orbital to an empty one and, thus, not constrained by the Pauli-exclusion principle (e.g., hole-doped F LaMnO₃).

FPLMTO calculations performed on YBaMn₂O₅ for P, F, and AF configurations show that the AF state has lower energy than the P and F configurations. Further, the spins are not canceled in the AF configuration and hence this state is really ferrimagnetic (Ferri). YBaMn₂O₅ is seen to be an indirect-band-gap semiconductor with a finite band gap of 0.88 eV. In the P and F cases finite DOS values are present in the vicinity of the E_F thus showing metallic behavior; the insulating behavior appears only when we introduce Ferri ordering in the calculations [158]. Unlike LaMnO₃ (where the energy difference between the F and *A*-AF cases is ~ 25 meV) [51] there is large energy difference (~ 0.5 eV) between the Ferri and F states of YBaMn₂O₅. So, a very large magnetic field is required to stabilize the F phase and induce an insulator-to-metal transition in YBaMn₂O₅. The stabilization of a Ferri ground state in YBaMn₂O₅ is consistent with the experimentally established magnetic structure [159]. The calculated magnetic moment at the Mn³⁺ site is $3.07 \mu_B$ and that at Mn²⁺ site is $3.91 \mu_B$ indicating that both Mn ions are in HS states.

In LaMnO₃ the spin ordering is found to be *A*-AF with the spins of the electrons coupled F in the *ab* plane and AF along the *c*-axis [51] which may be rationalized as follows. Due to the JT distortion of the MnO₆ octahedra the half-filled d_{z^2} orbitals in the *ab* planes order to give long and short Mn–O bonds, while the $d_{x^2-y^2}$ orbitals remain empty. Thus, within the *ab* plane, the superexchange is from a half-filled orbital on one atom to an empty one on a neighboring Mn atom leading to F coupling according to Hund's rule (viz. the transferred electrons prefer to have a parallel or antiparallel spin arrangement with respect to the receiving cation depending upon which state has the larger atomic spin). The superexchange between the half-filled d_{z^2} orbitals leads to AF coupling along *c*.

In YBaMn₂O₅, the Mn³⁺–O(1)–Mn²⁺ angle is 157.8° along the basal plane and the Mn³⁺–O(2)–Mn²⁺ angle is 180° in the apical direction. The large difference between these angles plays a key role in the magnetic properties. In YBaMn₂O₅ the real hopping of the d_{xy} , d_{xz} , and d_{yz} (t_{2g} -like) electrons between Mn³⁺ and Mn²⁺ produces a superexchange AF coupling. The exchange interaction between Mn²⁺ and Mn³⁺ along *c* is AF owing to the 180° bond angle which facilitates *p*–*d* σ bonding with the O(2)– p_z orbital and superexchange interaction [161].

With a bond angle of only 157° within the basal plane, the $d(\text{Mn})$ – $p(\text{O})$ covalent bond is weak and moreover due to the HS state of Mn³⁺ in the square-pyramidal crystal field, the $d_{x^2-y^2}$ orbitals at the Mn³⁺ site is almost empty whereas those at Mn²⁺ ion is half filled (see Fig. 12). Hence, the AF superexchange interaction between Mn²⁺ and Mn³⁺ within the basal plane is weaker than that along *c*.

The calculated exchange-splitting energy for Mn³⁺ and Mn²⁺ are 3.1 and 3.4 eV, respectively and this difference leads to incomplete cancellation of the spins on Mn(1)³⁺ and Mn(2)²⁺ despite the AF superexchange interaction between them, resulting in a Ferri state with a total magnetic moment of $0.85 \mu_B/\text{f.u.}$ If one considers the Goodenough–Kanamori [162] rules for magnetic interactions in manganese oxides, the expected magnetic order should be *A*-AF (viz. F ordering within the layers from the double-exchange interactions between occupied $d_{x^2-y^2}$ orbitals on Mn²⁺ and empty $d_{x^2-y^2}$ on Mn³⁺ and AF ordering between the layers from the superexchange interaction between half-filled d_{z^2} orbitals of Mn²⁺ and Mn³⁺). However, owing to the large deviation of the basal plane Mn–O–Mn bond angle from 180° along with the JT distortion for both Mn sites the $d_{x^2-y^2}$ orbital is not completely empty on Mn³⁺ (see Fig. 12) and consequently AF ordering is observed between Mn within as well as between the planes (see Fig. 11c). Thus, the competition between the superexchange and double-exchange interactions gives *G*-type Ferri ordering in YBaMn₂O₅ in accordance with the experimental findings [159].

2.9.2. Charge ordering

At low temperatures, manganese perovskites are characterized by strong competition between charge-carrier itinerancy and localization. Mixed-valent perovskite-like manganites are typically considered to be disordered with Mn³⁺ and Mn⁴⁺ ions randomly distributed in the lattice. However, under certain chemical and temperature conditions, and especially when Mn³⁺ and Mn⁴⁺ are present in equal amounts, these cations order coherently over long distances to form a CO lattice. Generally a transition to a CO AF state is preceded by a transition from an AF or P insulator to an F metal state at higher temperatures. Moreover, the CO state can readily be melted to F state by application of magnetic field [163], pressure [164] or exposure to X-ray photons [165].

Usually if the carrier-to-lattice coupling becomes stronger the tendency to CO becomes larger. The CO drastically influences the magnetic correlations in manganites. In the double-exchange picture, localized carriers cannot induce the F coupling. Investigations on CO have established the intimate connection between lattice distortion and CO. It is the lattice distortion associated with the OO that appears to initiate and

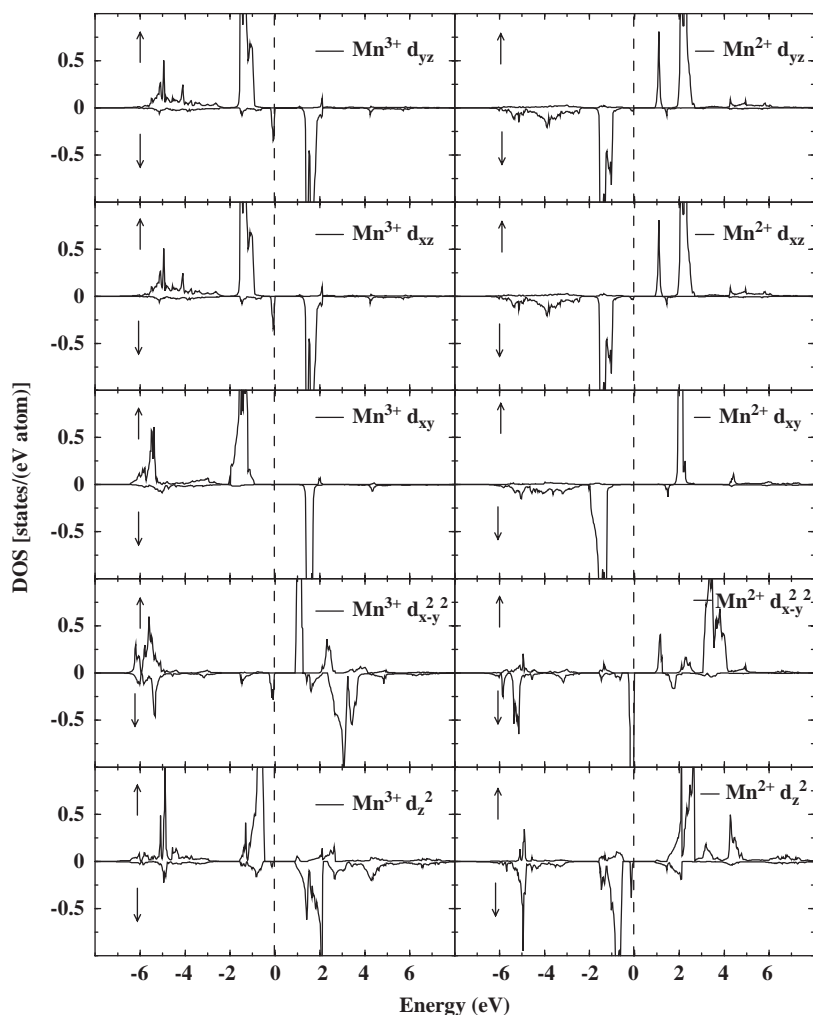


Fig. 12. Decomposed d -orbital DOS for Mn^{3+} (left panels) and Mn^{2+} (right panels) in Ferri state YBaMn_2O_5 obtained from the full-potential FLAPW method.

promote the CO. Eventually the Coulomb interaction wins over the kinetic energy of the electrons to form the long-range CO state. Resonant X-ray scattering measurements [166] show strong coupling between charge and orbital degrees of freedom for the d electrons of the manganites and hence CO and OO usually occur concurrently at the CO temperature (T_{CO}). Although the CO cannot be detected directly by neutron diffraction, the charge distinction (typically Mn^{3+} or Mn^{4+} in hole-doped perovskite-like oxides) is proportional to the spin moment ($S = 2$ vs. $S = 3/2$) and therefore the magnetic structure analysis indirectly confirms the CO state. A high magnetic field induces a melting-like phenomenon of the electron lattice of the CO phase giving rise to a huge negative magnetoresistance [167].

CO is expected to be favored for equal proportions of Mn^{2+} and Mn^{3+} as in (say) YBaMn_2O_5 where it is associated with the AF coupling between Mn atoms in the ab plane. CO depends on the d -electron-band width and hence it is worth to consider this feature in some

detail. On reduction of the Mn–O–Mn angle, the hopping between the Mn- $3d$ and O- $2p$ orbitals decreases and hence the e_g -band width decreases. Consequently the system stabilizes in a Ferri-CO-insulating state. The calculations for the F state provides metallic behavior [158]. Usually the CO-insulating state transforms to a metallic F state on the application of a magnetic field. This may be the reason for the metallic behavior of the F phase established by the calculations. Owing to the square-pyramidal crystal field acting on the HS Mn in YBaMn_2O_5 , d_{z^2} electrons are found in the top-most VB of Mn^{3+} , as compared with both d_{z^2} and $d_{x^2-y^2}$ electrons for Mn^{2+} (Fig. 12). Thus the distinction between Mn^{3+} and Mn^{2+} is clearly reflected in the different topology of their DOS curves. Consistent with the fact that the Mn^{3+} –O(1) bond length is 1.908 Å compared with 2.086 Å for Mn^{2+} –O(1), more electronic charge is present on Mn^{2+} than on Mn^{3+} . This is visible in the orbital decomposed DOS (Fig. 12), where the d_{xy} orbital of Mn^{2+} has more states (electrons) than that of Mn^{3+} .

The one-electron W or equivalently the e_g -electron-transfer interaction is governed by the degree of hybridization between the Mn-3d e_g state and the O-2p σ state which approximately scales with $\cos^2\alpha$ of the averaged Mn–O–Mn bond angle α . The double-exchange interaction arises from the itinerancy of the e_g electrons, and therefore the reduction in W favors the CO state, as well as destabilizes the F state. In manganites, the application of magnetic fields align localized t_{2g} -like electrons F (viz. a change from AF) and hence the double-exchange carriers gain mobility due to reduced spin scattering and result in a large reduction in resistivity at the AF-to-F transition point. This is the conventional magnetoresistance (MR) effect seen around the AF-insulating to F-metallic transition point. The manifestation of the CO state in conductivity measurements is a remarkable MR effect of up to six orders of magnitude change in resistivity at T_{CO} in, say, $\text{Nd}_{0.5}\text{Sr}_{0.5}\text{MnO}_3$ [163,167].

In order to visualize the presence of CO and Ferri spin ordering in YBaMn_2O_5 we show the calculated d -electron-density distribution for the Mn ions in the up- and down-spin channels in Fig. 11a and b, respectively. In the CO state of this material, the different Mn ions have different occupation as well as distribution of valence d electrons. This feature ensures that the spins do not cancel exactly, resulting in the Ferri ordering (Fig. 11c). The CO in YBaMn_2O_5 is characterized by the real-space ordering of Mn^{2+} and Mn^{3+} illustrated in Fig. 11a and b.

2.9.3. Orbital ordering

In transition-metal oxides with their anisotropically-shaped d orbitals, Coulomb interaction between the electrons (strong electron-correlation effect) may be of great importance. OO gives rise to anisotropic interactions in the electron-transfer process which in turn favors or disfavors the double-exchange and superexchange F or AF interactions in an orbital direction-dependent manner and hence gives a complex spin-orbital-coupled state. The tendency to CO and/or OO prevails in doped manganites, whereas OO otherwise occasionally accompanies the concomitant CO [168] in manganese oxides.

When the size of R and the alkaline-earth becomes smaller the one-electron W (and accordingly e_g -electron-transfer interaction) decreases [153]. For Y^{3+} with an ionic radius of 1.25 Å, [smaller than other R s like La^{3+} (1.36 Å) [169]] the Mn³⁺–O(1)–Mn²⁺ angle becomes much smaller than 180° and hence a reduction in the W as expected. The reduction in t by the lattice distortion and oxygen non-stoichiometry causes narrowing of the effective W of the e_g -like band, and such narrowing tends to destabilize the double-exchange F state due to the presence of competing processes, such as AF superexchange interaction between the localized spins,

CO, OO, and JT-type electron-lattice coupling [156]. In particular CO accompanied by a simultaneous ordering of the e_g -like orbitals promotes superexchange interactions. The anomalous X-ray scattering obtained by synchrotron radiation with the energy tuned to the resonant transition between 1s-core and 4p-unoccupied electronic energy levels provides direct evidence for the OO configuration [166]. The significant difference in the electron-density distribution between the Mn ions in Fig. 11a and b clearly indicates that there occurs two different valence states with different orbital structures.

In YBaMn_2O_5 there exist orbital degrees of freedom for the d_{z^2} electrons of Mn^{3+} and the d_{z^2} and $d_{x^2-y^2}$ electrons of Mn^{2+} , and OO can lower the electronic energy through the JT mechanism. The electron-lattice coupling induces a charge-localization tendency accompanied by structural distortions which eventually leads to CO and OO. Usually the reduction of the average size of the A atom in the perovskite-like compounds reduce W and in turn enhances the electron-lattice (collective JT) coupling. Therefore, mixed-valent manganites can have OO in addition to CO [170]. Owing to the HS state of Mn in the square-pyramidal environment in YBaMn_2O_5 the d_{z^2} orbital of Mn^{3+} and $d_{x^2-y^2}$ orbital of Mn^{2+} are half filled resulting in JT distortions for both kinds of Mn ions. In the square-pyramidal crystal field without JT distortions, the HS-state Mn^{3+} ions would have half-filled d_{z^2} orbital and completely empty $d_{x^2-y^2}$ whereas the HS-state Mn^{2+} ions would have the d_{z^2} and $d_{x^2-y^2}$ orbitals completely filled in one of the spin channels and completely empty in other. However, as a consequence of the JT distortion for both Mn ions, we find different Mn–O bond lengths. Further, due to the JT distortion a finite number of electrons are occupied in the $d_{x^2-y^2}$ orbitals of Mn^{3+} and there are appreciable electrons present in both spin channels for the d_{z^2} and $d_{x^2-y^2}$ orbitals of Mn^{2+} (Fig. 12). In YBaMn_2O_5 the electron–phonon interaction can arise from lattice distortions due to the different ionic size of Mn^{3+} and Mn^{2+} , and also the JT-type distortions for both kinds of Mn ions. The JT distortion is primarily responsible for the OO in YBaMn_2O_5 .

Neutron diffraction [159] indicates that Mn^{3+} has the occupied d_{z^2} orbital extending along [001], whereas the unoccupied $d_{x^2-y^2}$ orbital extends along [110] and $[1\bar{1}0]$. A corresponding OO could be expected for Mn^{2+} with both d_{z^2} and $d_{x^2-y^2}$ orbitals occupied. Detailed electronic structure studies show that due to JT distortion both d_{z^2} and $d_{x^2-y^2}$ orbitals have a finite filling for Mn^{2+} and Mn^{3+} (Fig. 12). In the bc plane the d_{z^2} orbital is ordered along c for both Mn^{3+} and Mn^{2+} , and this orbital hybridizes with the O(1)- p_z orbital resulting in σ bonding. There is zero overlap between the $d_{x^2-y^2}$ and p_z orbitals because of their different orientation in the ab plane. Therefore, the electron in the $d_{x^2-y^2}$ orbital can not hop along c . Moreover the direct overlap between O

$p_{x,y}$ and Mn d is small in the ab plane ($d_{x^2-y^2}$ is almost empty for Mn^{3+} and only partly occupied for Mn^{2+} due to the JT distortion) and hence the d electrons become localized and the CO and OO arise. In order to visualize the OO in YBaMn_2O_5 further we show in Fig. 11d the electrons distribution at the Mn sites between -1 eV and E_F (viz. the electrons mainly participating in the hopping interactions).

3. Excited state properties

3.1. Calculation of XES and XANES spectra

The theoretical X-ray absorption/emission spectra can be derived along the lines described by Neckel et al. [171] (within the dipole approximation) from the FLAPW [172] in terms of partial DOS. The intensity $I(\omega) = E - E_c$ arises as a result of transitions from initial VB states (energy E and angular momentum ℓ) to a final core state (E_c, ℓ') and is given by

$$\frac{I_{\tau n \ell'}(\omega)}{\omega^3} = \sum_{\ell} W_{\ell \ell'} M_{\tau}^2(\ell, n' \ell', E) D_{\ell}^{\tau}(E) \times \delta(E - E_{n' \ell'}^{\text{core}} - \hbar\omega), \quad (5)$$

where $M_{\tau}^2(\ell, n' \ell', E)$ is a matrix element and $W_{\ell \ell'}$ is the transition coefficient. In the case of absorption spectra $D_{\ell}^{\tau}(E > E_F) = 0$, and for emission spectra $D_{\ell}^{\tau}(E < E_F) = 0$. To account for the instrumental resolution and lifetime broadening of both core and valence states the calculated spectra have to be broadened, e.g., using a Lorentzian function with FWHM = 1 eV.

The X-ray emission spectra (XES) have been calculated for LaCoO_3 in LS, IS, and HS configurations and compared with resonant inelastic soft X-ray scattering spectra measured at different temperatures [152]. The calculated XES for LaCoO_3 in the LS state is found to be in good agreement with low-temperature experimental spectra. At higher temperatures the experimental spectra deviate considerably from the calculated spectra for the HS state, but are in excellent agreement with those for the IS state thus providing additional support for the inferred conclusion that LaCoO_3 transforms from the LS to IS state (see Section 2.8).

The X-ray absorption spectroscopy is a site-specific tool to probe the electronic structure of solids. From calculated spectra one can indirectly compare calculated electronic structures with experimental data, e.g., probe the CB in solids. Calculated $\text{OK}\alpha$ and $\text{MnK}\alpha$ spectra for the A -AF phase of LaMnO_3 are shown in Fig. 13. Because of the angular-momentum selection rule (dipole approximation), only O- $2p$ and Mn- $4p$ states contribute to the O- and Mn- K -edge spectra, respectively. The calculated X-ray absorption spectrum for the O K -edge (VB $\rightarrow 1s$) is given in the upper panel of Fig. 13 along

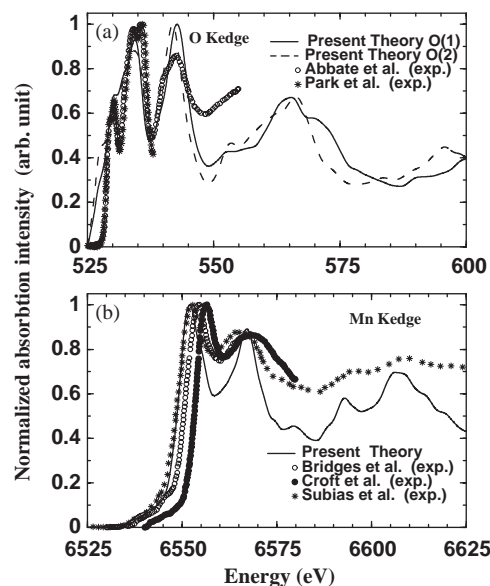


Fig. 13. The (a) O K -edge and (b) Mn K -edge XANES spectra for A -AF state LaMnO_3 with orthorhombic GdFeO_3 -type structure. Experimental Mn K -edge spectra are taken from Refs. [173–175] and O K -edge spectra from Refs. [176,177].

with available experimental spectra. The experimental spectra have two prominent peaks in the low-energy range and both are well reproduced in the theoretical spectra even without including the core-hole effect in the calculation. As manifested in different Mn–O distances, there are two (crystallographical) kinds of oxygens present in LaMnO_3 (see Section 2.4) which results in considerable differences in the peak positions in the XANES spectra (Fig. 13a).

The calculated Mn- K -edge spectrum for LaMnO_3 is given in Fig. 13b along with the available experimental spectra. The experimental spectra show two peaks in the lower-energy region and these are well reproduced in the theoretical spectrum. In particular the Mn- K -edge spectrum is found to be in very good agreement with that of Subias et al. [173] in the whole energy range considered. The good agreement between experimental and calculated XANES spectra further emphasizes the relatively little significance of correlation effects in LaMnO_3 and also shows that the gradient-corrected full-potential approach is able to predict even the unoccupied spectra quite correctly.

3.2. XPS, UPS, and BIS spectra

The electronic structures from DFT calculations can not be compared directly with measurements, but can be evaluated indirectly from experimental spectra. The experimental X-ray photoemission (XPS) and ultraviolet photoemission spectra (UPS) contain information about the VB electronic structure of solids.

In most cases the broadened DOS functions obtained from the DFT calculations are used for the comparison with experimental XPS, UPS or BIS spectra. However, in order to obtain a meaningful comparison with experimental studies it is important to include the appropriate momentum matrix elements involved in a particular scattering process. In this way the explicit calculation of XPS and UPS spectra will give more insight into the origin of the different features in the experimental spectra. The bremsstrahlung isochromat spectra (BIS) is a probe to study the electronic structure of unoccupied states for solids. For the evaluation of BIS one uses the unoccupied part of the DOS function instead of the occupied part (viz. VB).

Within the so-called single-scatterer final-state approximation [178,179] the photo-current is a sum of local (atomic-like), partial (ℓ -like) DOSs, weighted by the cross sections (transition probabilities). For high incident energies in XPS (~ 1.5 keV) the low-energy electron-diffraction function [179] can be simplified and the fully relativistic angle-integrated intensity [$I(E, \omega)$] can be written as

$$I(E, \omega) = \sum_{\tau} \sum_{\kappa} \sigma_{\kappa}^{\tau}(E, \omega) D_{\kappa}^{\tau}(E) \delta(E_F + \hbar\omega - E), \quad (6)$$

$$\kappa = \begin{cases} -\ell - 1, & j = \ell + \frac{1}{2}, \\ \ell, & j = \ell - \frac{1}{2}. \end{cases}$$

This expression has been cast into a Fermi golden-rule form, where $D_{\kappa}^{\tau}(E)$ are the partial DOS for the κ th channel at the τ th site, and are obtained from full-potential LMTO calculation. The relativistic cross sections $\sigma_{\kappa}^{\tau}(E, \omega)$ are calculated using the muffin-tin part of the potential over the energy range (E) of the DOS functions for the fixed incident photon energy ω . Because the cross sections (matrix elements) are energy dependent, the theoretically predicted spectra will depend on the energy chosen for the calculation. To be consistent with the reported XPS data, we have made calculations with fixed incident photon energy $\omega = 1253.6$ eV (MgK α line) for LaMnO₃ and 1486.6 eV (corresponding to AlK α source) for CaRuO₃. A finite lifetime of the photo-holes is taken into account approximately by convoluting the spectra using a Lorentzian with an energy-dependent half width. In addition to the Lorentzian lifetime broadening, the spectra were broadened with a Gaussian of half width 0.8 eV to account for the spectrometer resolution. With appropriate $\sigma_{\kappa}^{\tau}(E, \omega)$ the XPS and BIS spectra can be obtained from partial DOS functions ($E < E_F$ and $E > E_F$, respectively). By using a fixed incident photon energy of 21.2 eV [corresponding to an He(I) source] or 40.8 eV [corresponding to an He(II) source] one can obtain the respective UPS spectra.

The calculated VB XPS for *A*-AF LaMnO₃ is compared with the experimental spectrum [52] in

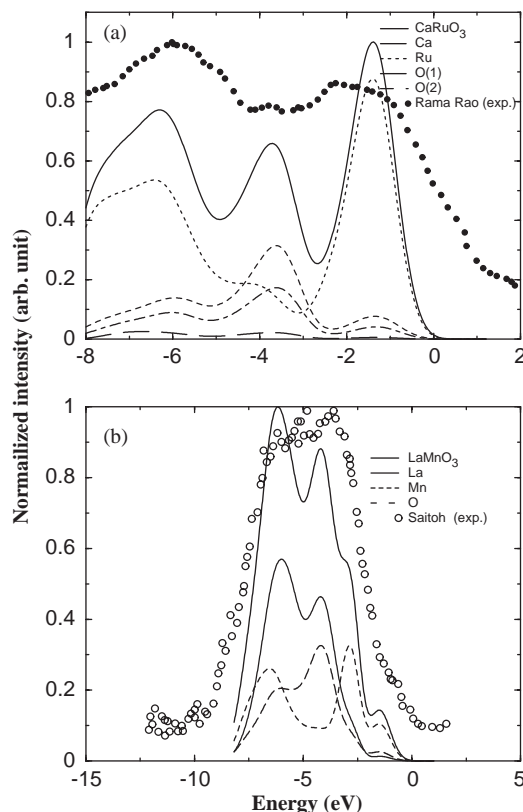


Fig. 14. Calculated XPS spectra for (a) *G*-AF CaRuO₃ and (b) *A*-AF LaMnO₃ and compared with the experimental spectra from Refs. [52,180].

Fig. 14b. The experimental XPS data show three peak-intensity features between -7 and -3 eV and these are well reproduced in the calculated profile. The large experimental background intensity makes a direct comparison with the calculated peak feature around -1.8 eV difficult. The overall agreement between the theoretical and experimental positions of peaks and shoulders in the XPS is very satisfactory. Note that the experimental XPS does not exhibit any appreciable intensity in the correlation-induced satellite at higher binding energies in contrast to the intense satellite features usually found in transition-metal monoxides (e.g., NiO). Thus, the good agreement between experimental and theoretical spectra indicates that the on-site Coulomb correlation effect is not significant in LaMnO₃.

The calculated XPS for the *G*-AF phase of CaRuO₃ in Fig. 14a shows that the peak features in the calculated spectrum agree extremely well with the experimental spectrum [180] over the entire energy range. As mentioned above, the intensity of the peaks depends upon the partial DOS as well as the cross-sections of the constituents of the compound. The first peak around -6 eV is mainly contributed by Ru-4d (e_g -like) electrons. The second peak at -4 eV reflects the combined contributions of the O-2p and Ru-4d electrons. The

prominent peak at ~ -1 eV is due to narrow Ru-4d (t_{2g} -like) electrons which are also responsible for the magnetism of this material. BIS spectra for LaMnO₃ and UPS spectra for CaRuO₃ obtained from the present type of calculations have recently also been compared [51,89] with experimental data.

3.3. Linear optical properties

Further insight into the electronic structure can be obtained by studying the optical properties. The optical functions reflect the fine structure of the energy distribution of the electron states in the VB and CB. The calculation of optical properties requires, apart from the Kohn–Sham eigenvalues, the explicit use of the wave functions, which therefore should be described as accurately as possible. In condensed matter systems, there are two contributions to the optical dielectric function [$\varepsilon(\omega)$], namely intra- and interband transitions. Contributions from intraband transitions are important only for metals and can be accounted for through the Drude relation with the use of (calculated) unscreened plasma frequencies. The interband transitions can further be split into direct and indirect transitions. The indirect interband transitions involve scattering of phonons and are neglected here. It is expected that the indirect transitions give only a small contribution to $\varepsilon(\omega)$ as compared with the direct transitions [181], although the indirect transitions will have a broadening effect and moreover depend on the temperature. Also other effects (neglected here) influence the optical properties, specifically, excitons normally give rise to rather sharp peaks at lower energies. The direct interband contribution to the imaginary part of the dielectric function [$\varepsilon_2(\omega)$] is calculated by summing all possible transitions from occupied to unoccupied states, taking the appropriate transition matrix elements into account, with appropriate broadening included. The real part of the components of the dielectric tensor $\varepsilon_1(\omega)$ are then calculated using the Kramer–Kronig transformation. The knowledge of both the real and imaginary parts of the dielectric tensor allows calculation of optical constants. Since the optical spectra are derived from the interband transitions, the microscopic origin of the peak structures can be rationalized in terms of the band structure.

In such computations, one goes beyond a minimal basis set and use a so-called double basis. Three different kinetic energies were used for each subset of the valence-electrons-derived bases of the basis set; two kinetic energies were used for bases derived from semicore and unoccupied states. A useful feature implemented in the FLMT0 [108] approach is the ability to incorporate basis functions derived from the same orbital quantum numbers with different principal quantum numbers in a single fully hybridizing basis set.

This feature entails the use of multiple sets of radial functions to represent bases with different principle quantum numbers. This capability is particularly useful in calculations of high-lying energy bands that must be used to obtain the dielectric functions at high energies.

The linear response of a system on an external electromagnetic field with a small wave vector can be described with the complex dielectric function $\varepsilon(\omega) = \varepsilon_1(\omega) + i\varepsilon_2(\omega)$. We have calculated the dielectric function for frequencies well above those of the phonons and therefore we have considered only electronic excitations. For these we used the random-phase approximation [182], neglecting local-field and finite-lifetime effects. Moreover, for noncubic structures the dielectric function is a tensor. By an appropriate choice of the principal axes one can diagonalize this tensor and restrict the considerations to the diagonal matrix elements. The interband contributions to the imaginary part of the dielectric functions $\varepsilon_2(\omega)$ are calculated by summing transitions from occupied to unoccupied states (with fixed \mathbf{k} vector) over the BZ, weighted with the appropriate matrix element to give the probability for the transition. To be specific, the components of $\varepsilon_2(\omega)$ are given by

$$\varepsilon_2^{ij}(\omega) = \frac{Ve^2}{2\pi\hbar m^2 \omega^2} \int d^3k \sum_{nn'} \langle \mathbf{kn} | p_i | \mathbf{kn}' \rangle \langle \mathbf{kn}' | p_j | \mathbf{kn} \rangle \times f_{\mathbf{kn}} (1 - f_{\mathbf{kn}'}) \delta(\varepsilon_{\mathbf{kn}'} - \varepsilon_{\mathbf{kn}} - \hbar\omega). \quad (7)$$

Here $(p_x, p_y, p_z) = \mathbf{p}$ is the momentum operator, $f_{\mathbf{kn}}$ is the Fermi distribution, and $|\mathbf{kn}\rangle$ the crystal wave function corresponding to the energy eigenvalue $\varepsilon_{\mathbf{kn}}$ with the crystal momentum \mathbf{k} . The evaluation of matrix elements according to Eq. (7) is performed over the muffin-tin and interstitial regions separately [183]. These calculations yield the unbroadened functions. The exact form of the broadening in the experimental spectra is unknown, although comparison with measurements suggests that the broadening usually increases with increasing excitation energy. Also the instrumental resolution smears out many fine features. To simulate these effects the lifetime broadening is simulated by convoluting the absorptive part of the dielectric function with a Lorentzian, whose full width at half maximum (FWHM) is equal to $0.01(\hbar\omega)^2$ eV. The experimental resolution is simulated by broadening the final spectra with a Gaussian (FWHM = 0.02 eV).

The calculated $\varepsilon_2(\omega)$ spectra for LaMnO₃, LaCoO₃, and LaNiO₃ are given in Fig. 15a along with available experimental results. Note that experimental $\varepsilon_2(\omega)$ spectra are not measured directly, but are derived from the Kramers–Kronig transformation of the measured reflectivity spectra. If one consider this fact also when comparing the calculated $\varepsilon_2(\omega)$ spectra with the experimental spectra one finds good agreement. This indicates that unlike earlier reported ε_2 spectra obtained from

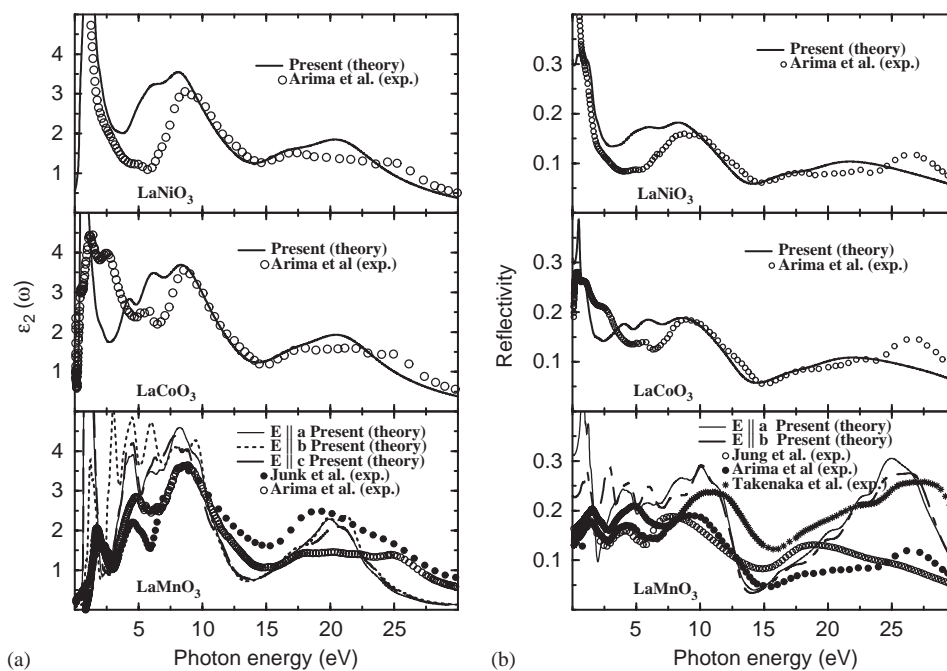


Fig. 15. (a) Imaginary part of optical dielectric tensors for the diagonal elements [$\epsilon_2(\omega)$] for the *A*-AF state LaMnO₃ with orthorhombic GdFeO₃-type structure and the “non-magnetic” phases of LaCoO₃ and LaNiO₃ with rhombohedral structure. (b) The corresponding reflectivity spectra for LaMnO₃, LaCoO₃, and LaNiO₃ with rhombohedral structure. Experimental reflectivity data for LaMnO₃ are taken from Refs. [185,55,186] and that for LaNiO₃ and LaCoO₃ are taken from Ref. [55].

ASA calculations [48,57], accurate full-potential calculations are able to provide the electronic structure of LaMnO₃ reliably not only for the occupied states but also for the excited states. Due to the orthorhombic structure of LaMnO₃ the dielectric function is a tensor. We have calculated the three components $E||a$, $E||b$, and $E||c$ of the dielectric constants corresponding to the electric field parallel to the crystallographic axes *a*, *b*, and *c*, respectively (lower panel in Fig. 15a), and the results show that there is considerable optical anisotropy present in LaMnO₃. Our calculations show [60,184] that compared to these perovskite-like oxides, systems such as SnI₂ and NaNO₂ possess large optical anisotropy. It is particularly interesting that for LaNiO₃, LaCoO₃, and LaMnO₃ the calculations correctly simulates the peaks around 2, 8, and 20 eV without the introduction of so-called scissor operations. This suggests that electron-correlation effects are not very significant in these materials.

After having evaluated the terms for ϵ_2 according to Eq. (7) one can derive the interband contribution to the real part of the dielectric function $\epsilon_1(\omega)$ from the Kramers–Kronig relation

$$\epsilon_1(\omega) = 1 + \frac{2}{\pi} P \int_0^{\infty} \frac{\epsilon_2(\omega') \omega' d\omega'}{\omega'^2 - \omega^2}. \quad (8)$$

In order to calculate $\epsilon_1(\omega)$ one needs to have a good representation of $\epsilon_2(\omega)$ up to high energies. Here 41 eV

above the E_F , was used for the truncation energy in Eq. (8).

The knowledge of both the real and imaginary parts of the dielectric tensor allows calculation of optical constants such as reflectivity, absorption coefficient, refractive index, extinction coefficient, electron energy loss spectrum, effective number of electrons involved in an optical transitions etc., as done for SnI₂ [60], NaNO₂ [184], LaMnO₃ [51], and manganese pnictides [187]. For example, the reflectivity spectra are derived from the Fresnel’s formula for normal incidence (assuming an orientation of the crystal surface parallel to the optical axes) as

$$R(\omega) = \left| \frac{\sqrt{\epsilon(\omega)} - 1}{\sqrt{\epsilon(\omega)} + 1} \right|^2. \quad (9)$$

From this approach the calculated reflectivity spectra for LaMnO₃, LaCoO₃, and LaNiO₃ are shown in Fig. 15b. For LaMnO₃ we have also given the experimentally measured reflectivity by Jung et al. [185], Arima et al. [55], and Takenaka et al. [186]. The reflectivity measured by Takenaka et al. [186] above 8.4 eV is found at a higher value than in the spectra of the two other experiments [55,185] (Fig. 15b). Overall our calculated reflectivity spectra are found to be in good qualitative agreement with the experimental spectra up to 30 eV. The peaks around 10 and 25 eV in the calculated spectra concur with the findings of

Takenaka et al. [186] and the optical anisotropy of LaMnO_3 is also clearly visible in the reflectivity spectra. In the case of LaCoO_3 and LaNiO_3 the calculated reflectivity spectra are compared with the corresponding reflectivity spectra measured by Arima et al. [55].

The very good agreement between the experimental and theoretical optical spectra indicates that this kind of theoretical approach well describes not only the occupied and unoccupied parts of the electronic structure but also the character of the bands. Further, as the optical properties arise from electronic interband transitions, the origin of the peaks in the experimental optical spectra can be explained from calculated band structures through optical interband transitions (see, e.g., Refs. [51,60,184]).

3.4. Magneto-optical properties

The investigation of compounds with high MO activity is of great importance both for applications (the search for potential materials for MO disks) and for achieving a deeper understanding of the electronic structure and magnetic properties of solids. Although MO properties of magnetic metals have been known for over 150 years [188], it is only in the past couple of decades that vigorous interest has been focused on this subject [189]. One reason is the potential for application in the technology of high-density data storage [190]. The MO effects such as Kerr effect, Faraday effect, and circular dichroism all have the common feature that they are due to a different interaction of left- and right-hand circularly polarized light with a magnetic field. The symmetry between left- and right-hand circularly polarized light is broken due to the SO coupling in a magnetic solid. This leads to different refractive indices for the two kinds of circularly polarized light, so that after reflection the sum of the two circular light components is not linearly polarized anymore, but tilted to elliptically polarized light. With the advent of modern relativistic energy-band theory [187,191–194] it has become possible to study the MO properties of solids quantitatively.

One of the goals of theoretical MO studies is to understand the appearance of large MO effects from aspects of the band structure, with the aim to predict suitable MO materials and at the same time disclose the limitations of the current MO theory. The present approach is essentially band-structure oriented using the Kohn–Sham energy bands of the material to evaluate the optical spectra in a linear-response formalism. The Kerr effect can be expressed in terms of the optical conductivity tensor σ [195], which in its explicit expression depends on the geometry of the incident-light wave vector, the orientation of the magnetic moment, and the surface normal. Of these, the polar Kerr effect (for which the direction of the macroscopic

magnetization of an F material and the propagation direction of the linearly-polarized incident-light beam are perpendicular to the studied surface planes) is the most widely used geometry in technological applications. Hence, we have limited our theoretical investigations to the polar Kerr effect. With the magnetic moment in the [001] direction of an uniaxial crystal, the form of the optical conductivity tensor is

$$\sigma = \begin{pmatrix} \sigma_{xx} & \sigma_{xy} & 0 \\ -\sigma_{xy} & \sigma_{xx} & 0 \\ 0 & 0 & \sigma_{zz} \end{pmatrix}. \quad (10)$$

Consider a plane-polarized light beam traveling in the z direction which is defined parallel to the magnetization direction \mathbf{M} . This light beam can be resolved into two circularly polarized beams with the spinning direction of the corresponding electric field parallel and antiparallel to \mathbf{M} . The sign convention ascribes a positive sign to a cube in which right-circular polarized (RCP) light has its electric-field vector \mathbf{E} clockwise rotated at a given point in space. In other words a positive value implies a clockwise rotation of the axes of the polarization ellipse, as viewed by an observer who looks in the $+z$ direction with the incoming linearly polarized light traveling along the $+z$ direction [the sign convention being the same for the Kerr (θ_K) and Faraday rotation (θ_F)]. In polar geometry, the Kerr-rotation (θ_K) and ellipticity (η_K) are related to the optical conductivity through the relation:

$$\frac{1 + \tan(\eta_K)}{1 - \tan(\eta_K)} e^{2i\theta_K} = \frac{(1 + n_+)(1 - n_-)}{(1 - n_+)(1 + n_-)}, \quad (11)$$

where n_{\pm}^2 in terms of conductivities are

$$n_{\pm}^2 = 1 + \frac{4\pi i}{\omega} (\sigma_{xx} \pm i\sigma_{xy}). \quad (12)$$

For small Kerr angles, Eq. (11) can be simplified [196] to

$$\theta_K + i\eta_K = \frac{-\sigma_{xy}}{\sigma_{xx} \sqrt{1 + (4\pi i/\omega)\sigma_{xx}}}. \quad (13)$$

The magnetic circular birefringence (viz. the Faraday rotation), describes the rotation of the polarization plane of linearly polarized light on transmission through matter magnetized in the direction of the light propagation. Similarly, the Faraday ellipticity (η_F), which is also known as the magnetic circular dichroism, is proportional to the difference between the absorption for right- and left-handed circularly polarized light [188]. These quantities are related [197] by:

$$\theta_F + i\eta_F = \frac{\omega d}{2c} (n_+ - n_-), \quad (14)$$

where c is the velocity of light in vacuum, and d is the thickness of the (thin-film) material. Because of the metallic nature of F materials the optical spectra in the lower energy range will have a dominant contributions

from intraband transitions whereas contribution to the diagonal components of the conductivity is normally described by the Drude formula [198]

$$\sigma_D(\omega) = \frac{\omega_P^2}{4\pi(\frac{1}{\tau} - i\omega)} \quad (15)$$

The relaxation time τ , characterizing the scattering of charge carriers, is dependent on the amount of vacancies and other defects, and will therefore vary from sample to sample. The unscreened plasma frequency (ω_P) depends on the concentration of the charge carriers and we have calculated the spin-resolved unscreened plasma frequency by summing over the Fermi surface using the relation

$$\omega_{Pii}^2 = \frac{8\pi e^2}{V} \sum_{\mathbf{k}\eta} \langle \mathbf{k}n\xi | p_i | \mathbf{k}n\xi \rangle \langle \mathbf{k}n\xi | p_i | \mathbf{k}n\xi \rangle \delta(E_{\mathbf{k}n\xi} - E_F), \quad (16)$$

where V is the volume of the primitive cell, e the electron charge, and ξ the spin. The ω_P were calculated using the FLAPW method and the above relation using a sufficiently large number of \mathbf{k} points.

In addition to their excellent MO properties, several bilayer materials possess large perpendicular magneto-crystalline anisotropy at room temperature (a necessary condition for the practical use of the polar Kerr effect in a read-out process) [106], and such materials have therefore been extensively investigated also as candidates for MO recording media. Studies of the MO Kerr effect (MOKE) offer unique insight into the spin-polarized electronic structure of magnetic materials because MOKE is most sensitive to those parts of the band structure which initially give rise to magnetism. A systematic study of such materials is expected to give more insight into the physical origins of large MO effects, and may thus aid in identifying the interactions that are the most crucial for the design of materials with desired MO properties. Recent studies by Mohn et al. [199] show that if the material has strongly aspherical spin density, a full-potential treatment is important in order to achieve the correct magnetic ground state. Since the MO properties arise from the exchange splitting in combination with SO coupling, the results of Mohn et al. suggest that the full-potential treatment may be important in order to describe the MO properties properly. In addition calculation of MO properties requires an accurate description of the Kohn–Sham eigenvalues and eigenvectors, which also is a motivation in itself for the use of a full-potential method [187].

The calculated Kerr rotation spectrum for FePt is shown in Fig. 16 along with several experimental (with large mutual differences) and theoretical results available in the literature. Usually experimental measurements show appreciable variations in the Kerr spectra with temperature [200,201]. Theoretical spectra corre-

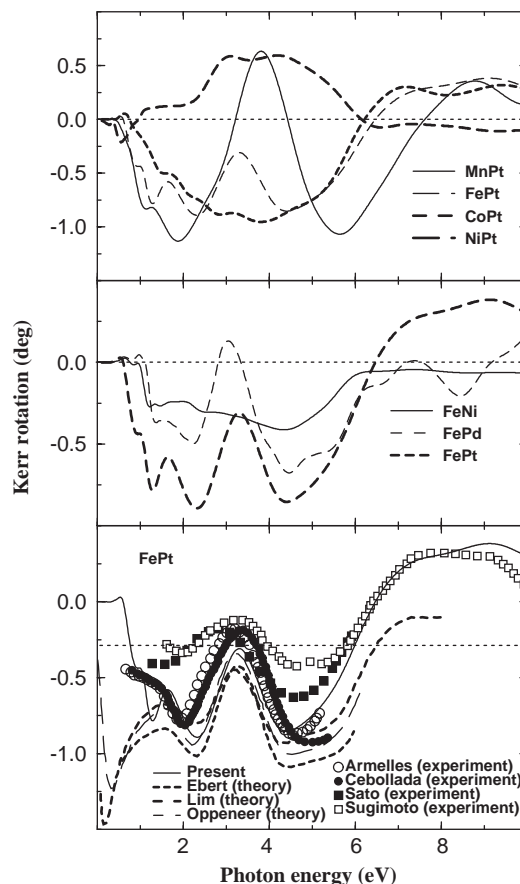


Fig. 16. Calculated MOKE spectra for selected bilayer materials. The lower panel for FePt also includes theoretical data from Refs. [210,204,205] and experimental data from Refs. [202,203,211,212].

spond to 0 K and hence one can only make reasonable comparison with experiments when low temperature data are available. MOKE spectra for FePt prepared at different conditions [202] show large variation with the crystalline perfection of the samples, large MOKE being only observed for well crystalline specimens. Taking these facts into account there must be said to be largely excellent agreement between experimental and theoretical result. Few experimental studies have been reported concerning MO effects beyond 6 eV due to the high absorption of quartz optical devices used in MO apparatus and the requirement of high-vacuum-compatible magnet systems. In order to investigate the contributions from Fe and Pt for the MO properties of FePt Sugimoto et al. [203] measured the MOKE spectra in the photon energy range 1.55–10.5 eV. Our calculated Kerr rotation spectra for FePt is found to be in excellent agreement with the experimental results of Sugimoto et al. from 6 to 10 eV. Hence the present type of theoretical approach can be used to predict the MO properties of materials at higher energies.

The present ab initio calculation has taken into account both inter- and intraband contributions to the

MO properties whereas earlier calculations [204,205] did not take into account the intraband contributions (which dominates in the infrared region; $h\nu = <1.5$ eV). There is accordingly a large deviation between the present result and the earlier calculations in the lower energy range (Fig. 16). In general, the orbital and spin magnetic moments largely contribute to the MO effects [206]. Those of 3d transition metals strongly depend on the atomic coordination number [207], the SO interaction on d electrons [208], and in their binary 3d-metal alloys the symmetry of d -wave functions [209]. In order to understand the role of SO interactions on MO properties we show the trend in the calculated Kerr spectra of FeNi, FePd, and FePt in the middle panel in Fig. 16 where an increase in the magnitude of the peaks around 2 and 4 eV with increasing atomic number is seen. The SO-interaction parameter ξ increases from 122 meV for Ni to 660 meV for Pt. Since the SO-coupling strength grows with increasing atomic number, it is quite reasonable to assign the trend seen in the middle panel of Fig. 16 to increasing SO coupling. When we go from NiPt to MnPt the magnetic moments increases from 0.61 to $4.02 \mu_B$ and correspondingly the exchange-splitting energy increases. In order to understand the role of exchange splitting on MO properties we give the calculated Kerr rotation spectra for X Pt ($X = \text{Mn, Fe, Co or Ni}$) in the F phase in the top panel of Fig. 16 which shows that the magnitude of the Kerr rotation spectra at 2 and 4 eV decreases on going from MnPt to NiPt. The variation in atomic number of the X component is small, whereas the appreciable variation in magnetic moment, and hence the exchange splitting may provide an explanation for the changes in the Kerr rotation spectra. However, the variation is not systematic in the whole photon-energy range and the details show that MO properties depend much on finer features of the band structure. Hence, straightforward empirical “rules of thumb” cannot be applied to improve MO materials and a first-principle computational approach may prove more valuable.

The MO effects can be studied either in transmission (Faraday effect) or in reflection (Kerr effect) mode. The Faraday effect can only be explored experimentally for sufficiently thin films. Further, the occurrence of multiple reflections due to Faraday rotation in the substrate, and discontinuous polarization changes at the various interfaces, complicates the investigation of the Faraday effect. Consequently, rather little work, experimental as well as theoretical, has been devoted to the Faraday effect compared to the Kerr effect. The few experimental results for the Faraday effect show large mutual differences and appear to strongly depend on the quality of the films [214]. Therefore, it is of general interest to calculate Faraday spectra for ideal crystals. The calculated specific Faraday rotation spectra for FePd and FePt are given in Fig. 17 along with the available

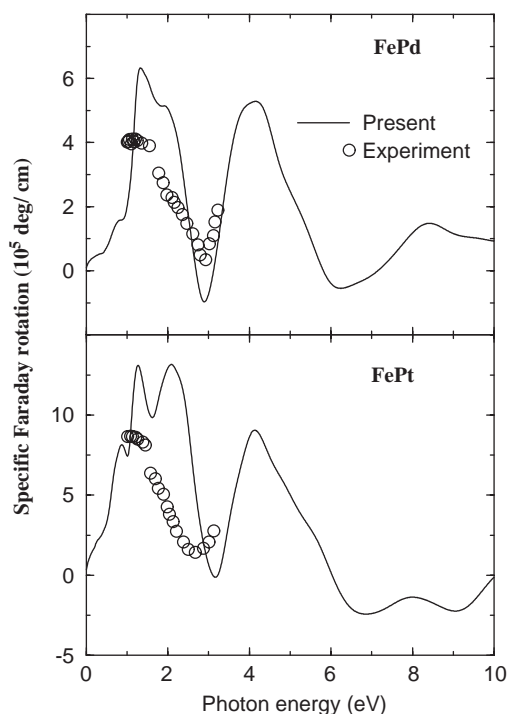


Fig. 17. Calculated MO Faraday rotation spectra for FePd and FePt in relation to experimental data [213].

experimental spectra [213]. The minimum Faraday rotation occurs around 3 eV for both compounds and the maximum is in the near IR region consistent with experimental observations. Overall the calculated specific Faraday rotation is smaller than experimentally established, but at least a part of these discrepancy may be attributed to effects of film thickness [213].

3.5. Phonons and Raman spectra

An atom in a solid is continuously oscillating about its equilibrium position with an energy which is determined by the chemical environment of the atom. Such lattice vibrations or phonons contributes to a large number of physical properties, such as the specific heat, optical and dielectric properties, electrical resistance, thermal expansion, etc. For this reason it is of interest to theoretically determine eigenfrequencies and eigenvectors of phonons from first-principle theory. As the adiabatic approximation provides a clear and physically founded framework to separate the motion of the electrons from the dynamics of the nuclei, the potentials governing the lattice vibrations can be established by the so called frozen-phonon technique [215]. In practical terms, one must first set up a supercell commensurate with the wave vectors of the phonons. The next step is to slightly displace the nuclei in this supercell from their equilibrium location in accordance with the translational requirements of the phonon modes. The total energy of the crystal is then calculated for this frozen-in

structural configuration. Repeating the calculation for a whole series of different displacements will yield a set of discrete total-energy values which are subsequently fitted to a polynomial function around the equilibrium structure to obtain the phonon potentials. In general excellent agreement is found between the thus derived phonon frequencies and the corresponding experimental data for all types of materials.

Raman scattering provides valuable information about the phonons, and in particular, highlight the interaction between the motion of atoms and the electronic subsystem. Raman scattering is based on a change in the polarizability and susceptibility of a crystal caused by quasi-particles. Hence, the modulation of the dielectric function ϵ by phonons gives rise to the observed Raman effect. The current stage of development in theory is to calculate Raman spectra from parameters which can be directly obtained from frozen-phonon ab initio band-structure calculations and allows one to take into account the anharmonicity of the lattice-dynamical potential [216]. Thereby all the required quantities can be obtained by first-principles band-structure methods within the frozen-phonon approach, where the total energy and dielectric tensor (as a function of atomic coordinates) are the main ingredients.

We have calculated IR and Raman active phonons for the superconducting and non-superconducting RT_2B_2C compounds. Siegrist et al. [217] found that the crystal structure of RT_2B_2C represents a filled-up variant of the well-known tetragonal $ThCr_2Si_2$ -type structure, where a carbon atom occupies the vacant $2b$ position in the R plane. This structure is highly anisotropic ($c/a \approx 3$) with alternate stacking of NaCl-type (RC) and inverse PbO-type (T_2B_2) layers. Phonon frequencies are studied at the Γ point in the BZ within the harmonic approximation. In the treatment of lattice dynamics, the frequencies at the Γ point are calculated from the dynamical matrix obtained using forces corresponding to different sets of linearly independent displacements of the atoms in the unit cell. The frozen-phonon calculations require knowledge of the phonon displacement patterns which entail a symmetry sorting of the vibrational spectra. At the zone center (Γ), the acoustic modes with symmetry $\Gamma_{ac} = A_{2u} + E_u$ have zero frequencies. The irreducible representations of the optical modes are

$$\Gamma_{op} = A_{1g}^{Raman} + B_{1g}^{Raman} + 2E_g^{Raman} + 3A_{2u}^{IR} + 3E_u^{IR} \quad (17)$$

Here, the subscripts g and u represent symmetric and antisymmetric modes with respect to the center of inversion. Since our unit cell has a center of inversion, there are only four Raman-active modes with a non-zero Raman-tensor element. The A_{1g} , B_{1g} , and E_{2u} modes have inversion symmetry and are thus Raman active.

The phonon frequencies are derived from frozen-phonon calculations, i.e., distortions (u) consistent with

the symmetry of the mode in question are introduced and the corresponding total energy is calculated. If we introduce the off-equilibrium displacements u_s of the atoms under consideration, a Taylor expansion of the total energy around the equilibrium positions in terms of the displacements can be written as

$$E(u_s) = E^{(0)} + \frac{1}{2} \sum_{ij} E_{ij}^{(2)} u_i u_j + \frac{1}{6} \sum_{ijk} E_{ijk}^{(3)} u_i u_j u_k + \dots \quad (18)$$

Here, the summations run from $i = 1$ to $3n$, where n denotes the number of atoms in the unit cell. Note, that we have assumed $q = 0$ phonons and are therefore able to drop the unit-cell index for the displacements and expansion coefficients. By making use of the undistorted crystal symmetry, the above expansion for the $3n$ degrees of freedom converts into several separate equations for each irreducible representation. The total energies were calculated for five different distortions for the A_{1g} mode, five for B_{1g} , 9 for E_g , and 12 for A_{2u} and E_u modes, using a maximum amplitude of displacement of approximately 0.04 Å.

The second derivatives required for the force-constant matrix elements were obtained by calculating the forces exerted on all atoms when one or two of the atoms are displaced in the a , b or c direction. Both positive and negative displacements were considered to take into account possible anharmonic effects. For all the frozen-phonon calculations we have used the experimental structural (equilibrium) parameters [218,219]. In the special case where the block size of the irreducible representation is 1, the calculated total energy as a function of u can be fitted with a simple polynomial

$$E(u) = E^{(0)} + a_2 \left(\frac{u}{L}\right)^2 + a_3 \left(\frac{u}{L}\right)^3 + \dots, \quad (19)$$

where L is the lattice parameter which is a for E_g and E_u modes and c for A_{1g} , B_{1g} , and A_{2u} modes. The coefficient a_2 in the second-order term of Eq. (19) is the harmonic contribution to the total energy, naturally referred to as a force constant. Knowing this, we then obtain the phonon frequency ω_{ph} as

$$\omega_{ph} = (2\pi L)^{-1} \left[\frac{a_2}{2\mu} \right]^{1/2}, \quad (20)$$

where μ is the mass of the atom which is involved in a given phonon mode.

Earlier studies [226,227] show that calculated vibrational frequencies by the GGA are in better agreement with experimental data than those obtained by the LDA. So all the results referred to are obtained from GGA calculations. The calculated Raman-active phonon frequencies for the RT_2B_2C compounds are given in Table 6 along with available experimental values from Raman-scattering [221–224] and inelastic neutron scattering experiments with Born–von Karman (BvK)

Table 6

Raman-active phonon frequencies (in cm^{-1}) for RT_2B_2C compounds obtained from FLMTO and FLAPW methods in comparison with available experimental data

Mode	YCo ₂ B ₂ C	YNi ₂ B ₂ C	LaNi ₂ B ₂ C	LuNi ₂ B ₂ C
B A_{1g} (FLAPW)	766	821	826	869
B A_{1g} (FLMTO)	799	830,893 [220]	890	875
B A_{1g} (Exp.)		813 [221], 832 [222], 847 [223], 823 [224]	833 [221]	863 [224]
B A_{1g} (Theo.)		825 [225]	818 [225]	
Ni or Co B_{1g} (FLAPW)	232	184	185	188
Ni or Co B_{1g} (FLMTO)	237	200,199 [220]	189	193
Ni B_{1g} (Exp.)		199 [221], 198 [222], 193 [224]	181 [221]	190 [224]
Ni B_{1g} (Theo.)		201 [225]	180 [225]	
Ni or Co E_g (FLAPW)	251	271	207	300
Ni E_g (Exp.)		287 [221], 282 [222], 273 [225]	208 [221], 203 [225]	
B E_g (FLAPW)	448	447	449	461
B E_g (Exp.)		460 [221], 470 [222], 439 [225]	441 [221], 419 [225]	

model evaluation [225]. The calculated A_{1g} - and B_{1g} -phonon frequencies are also comparable (see Table 6) with the frequencies obtained by Weht et al. [220] from the FLMTO method. The overall very good agreement between the experimental and our theoretical values indicates the reliability of the predicted values for the other modes and compounds. The polarization dependent Raman-mode measurements [224] on LuNi₂B₂C with ¹⁰B substituted for ¹¹B indicate that the mode near 830 cm^{-1} is due to the vibration of the B atoms, an inference confirmed by the theoretical study. The A_{1g} mode involves vertical B displacements that stretch/compress the linear B–C–B bonds while bending the B–Ni–B bond angles in the NiB₄ tetrahedron. The stiffness of the A_{1g} frequency reflects the strong B–Ni and B–C bonds consistent with chemical bonding analysis [228]. The calculated Raman-active phonons are found to be in good agreement with the experimental values indicating that GGA calculations can accurately predict the static density response and that phonons are not heavily dressed by spin or excitonic fluctuations in these borocarbides. Park et al. [224] could not identify the Ni- E_g and B- E_g modes from polarization dependent Raman measurements on RNi₂B₂C single crystals. However, our calculated phonon frequencies of the Ni- E_g and B- E_g modes for YNi₂B₂C are found to be in excellent agreement with the phonon frequencies obtained by the Raman-scattering measurements of Hadjiev et al. [222] and Hartmann et al. [221] which should clarify the controversy between the three reports.

A key feature is to compute Raman intensities for each of the vibrational modes directly within the GGA. The Raman-scattering activity associated with a given vibrational mode is related to the change in the electrical polarizability of the material due to the normal-mode displacements of the involved atoms [229]. The band structure and dielectric function for different displacements of the atoms have been determined employing the FLAPW method. These data have been used to evaluate

the derivatives of the dielectric function with respect to the displacements, which in turn are used to determine the corresponding Raman intensities [$I(\omega)$] which for a given mode is related to the derivative of the dielectric function (ϵ) with respect to the normal coordinate q_i of the vibration [216,230]

$$I(\omega) = \frac{\sum_i \exp\left(\frac{-\hbar\omega_i}{k_B T}\right) \sum_f |M_{if}|^2 L(\omega, \omega_i, \omega_f, \gamma)}{\sum_i \exp\left(\frac{-\hbar\omega_i}{k_B T}\right)}. \quad (21)$$

Here, ω_i denotes the phononic eigenvalues, $L(\omega, \omega_i, \omega_f, \gamma)$ accounts for a broadening of the transitions, and the matrix element M_{if} is given by

$$M_{if} = \frac{\partial \epsilon}{\partial q_i} \langle f | q_j | i \rangle, \quad (22)$$

where $|i\rangle$ and $\langle f|$ denote the initial and final vibrational state, respectively. We have computed ϵ for five points along each normal coordinate and fitted the q_i dependence of ϵ at the chosen frequency of incident light. All modes are almost harmonic, therefore the vibrational states $|i\rangle$ and $\langle f|$ are eigenstates of the harmonic oscillator.

From the derivative of the optical dielectric function with normal coordinates for phonon modes we have calculated the intensities of all the Raman-active mode of, say, superconducting YNi₂B₂C with a laser wavelength of 514.5 nm (Fig. 18). It is seen that the intensity of the E_g modes is much weaker than that of the A_{1g} mode and this may be a reason for the problem to observe the E_g mode in some of the experimental investigations [224]. The phonon frequency of the heavier Ni atom is expected to be lower than that of B and C (Fig. 18) and consistent with this expectation that the Ni- B_{1g} mode has the lowest frequency. We have also calculated Raman intensity as a function of laser energy for different polarizations. The overall Raman intensity is found to be high for laser energies around 2.5 eV. So, with a proper selection of a laser source operating in this energy range one can obtain better yield of

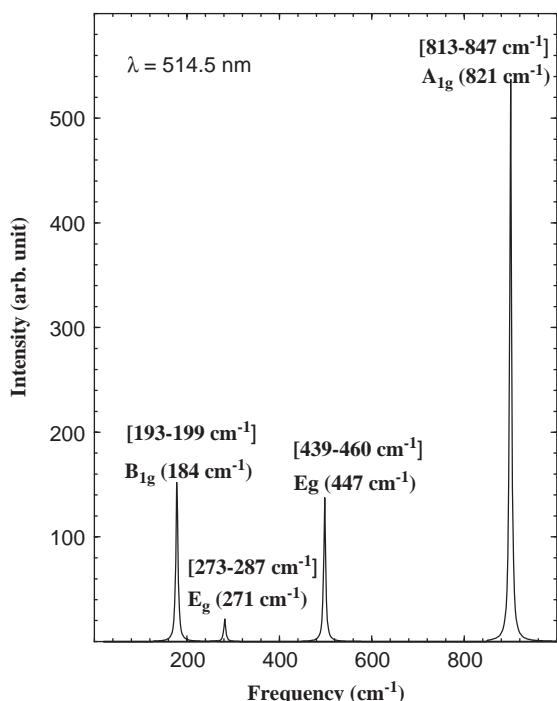


Fig. 18. Calculated Raman spectra for superconducting $\text{YNi}_2\text{B}_2\text{C}$. Phonon frequencies in parentheses are obtained from first principle frozen phonon calculation. The range of experimental phonon frequencies [221–224] are given in square brackets.

Raman-scattering intensity for these materials. Further we have detected a huge difference in the Raman intensity between different polarizations. In particular for the A_{1g} and B_{1g} modes the Raman intensity in the zz polarization is much smaller than that in the xx polarization. More details about our Raman spectra calculation can be found elsewhere [231].

4. Summary

The combination of experimental and theoretical data allows one to form an increasingly detailed physical picture of the basic interactions that determine the physical and chemical properties of solids. Apart from the gain in basic scientific knowledge, this will also help to approach the goal of designing new materials with properties optimized for technological applications.

With the combination of charge density, charge transfer, electron localization function, and crystal-orbital-Hamilton-population analyses one can distinguish different types of chemical bonding in complex materials such as ternary metal hydrides. The present type of theoretical approach is quite successful in predicting structural properties of hydrides and also the anisotropic structural changes upon hydrogenation. $\text{RTInH}_{1.333}$ constitutes a series with much shorter H–H separations than other known metal hydrides. The shortest distances between the H atoms in such metal

hydrides are governed primarily by the polarization of negative charges on H towards the positively charged La and In and also the R in the bipyramidal configuration acts as a shielding and to some extent compensates the repulsive H–H interaction. The conclusion drawn from this study is probably of more general validity, and may be utilized to search for other metal hydrides of potential interest for hydrogen storage purposes.

One can also reliably use the present type of theoretical examination to understand the phase stability of metal hydrides at high pressures. For example the ground state of $\alpha\text{-MgH}_2$ becomes unstable at higher pressure and the calculated transition pressures for α -to- γ - and γ -to- $\beta\text{-MgH}_2$ are found to be in very good agreement with the experimental findings. It is predicted that further compression of $\beta\text{-MgH}_2$ will lead to a phase transition to $\delta\text{-MgH}_2$ at 6.73 GPa and that the AlAu_2 -type structure of a hypothetical ϵ modification stabilizes above 10.26 GPa. The small energy differences suggest that the formation of the high-pressure ϵ -phase could also be possible at ambient pressure/temperature by choosing an appropriate preparation method. These high-pressure phases may increase the relative weight of stored hydrogen.

Single-crystal elastic constants can be obtained from first principles total energy calculations with good accuracy, if one includes gradient correction along with atomic relaxations into the calculations. Elastic properties can be reliably predicted with such an approach in cases where experimental determination is hampered by practical difficulties. From the calculated elastic constants one can derive the elastic properties such as bulk modulus, Young's modulus, shear modulus, Debye temperature, etc. As an example we have considered mechanical anisotropy in the aerospace engineering material Ti_3Al from the single-crystal elastic constants and found that the anisotropy is small in this material.

From systematic studies on a series of perovskite oxides we have found that one can get the correct insulating ground state of such materials only on including the proper magnetic ordering and structural distortions into the calculations in addition to the full-potential treatment. Even though the calculated band gaps are found to be underestimated by the present type of theoretical approach, it correctly provides the insulating behavior in charge-transfer insulators such as LaMnO_3 , LaFeO_3 , and LaCrO_3 . However this approach fails to predict the insulating behavior in Mott insulators such as LaVO_3 and LaTiO_3 in spite of the correct antiferromagnetic ordering and magnetic moment. This indicates that even the generalize-gradient-corrected full-potential linear muffin-tin orbital method is inadequate to treat the correlation effects in Mott insulators. So, one has to go beyond the standard local spin-density approximation to describe the ground state of Mott insulators correctly.

The relative strengths of the ferro- and antiferromagnetic exchange interactions in $\text{Sr}_{1-x}\text{Ca}_x\text{RuO}_3$ can be modified by varying the Ca content. On the basis of combined experimental and theoretical data we conclude that the ground state of CaRuO_3 must involve a spin-glass situation with short-range antiferromagnetic interactions.

To illustrate the magnetic properties of lanthanides and actinides we refer to calculations on cerium and uranium chalcogenides using different levels of approximations. It is found large orbital moments in all these chalcogenides which are antiparallel to the spin moments. Both local density approximation and generalized-gradient approximation calculations are unable to give the correct total magnetic moment in these systems. However, we found that inclusion of the orbital polarization correction to either the local-density approximation or generalized-gradient approximation calculations provides orbital moments matching those obtained by neutron diffraction measurements. Owing to the localization of f electrons, the spin, orbital, and total moments are enhanced on going from sulfides to tellurides. The lesson is that it is important to include orbital-polarization corrections in the density-functional calculations to predict magnetic properties of lanthanides and actinides correctly. The calculations also show that when one includes orbital-polarization correction to the local spin-density approximation one can predict the magnetic anisotropy in solids. It is indeed the combined effect of large crystal-field splitting (by structural distortions), exchange splitting, and spin-orbit splitting (for at least one of the constituents) which leads to large magnetic anisotropy in solids.

From fixed-spin total-energy studies as a function of hole doping and temperature using the generalized-gradient-corrected full-potential linear augmented plane wave method we have established the metamagnetic behavior of LaCoO_3 . The non-cooperative magnetic solution with Co^{3+} in the LS state has the lowest total energy at low temperature in accordance with experimental observations. From the energetics of different spin states it is established that the likely spin-state transition in LaCoO_3 is from LS to IS and the calculations show that the stabilization of a HS state in LaCoO_3 is less probable. Hole doping induces ferromagnetism in LaCoO_3 which originates from partial filling of the $\text{Co-}t_{2g}$ levels and which in turn leads to stabilization of an intermediate state over the low-spin ground state. This kind of approach can be used to study metamagnetism and spin-state transition in solids.

A close interplay among the spin, charge, orbital, and lattice degrees of freedom in manganites produces intriguing phenomena such as magnetic-field-induced insulator-metal transition and colossal magneto-resistance effect. In manganites there is a competition

between charge-ordered (insulating) antiferro-/ferromagnetic superexchange interaction and the ferromagnetic (metallic) with the double-exchange interaction which changes with effective one-electron band width, hopping interaction between Mn and O, the valence of Mn ions, and carrier concentrations. The presence of spin, charge, and orbital ordering in insulating ferromagnetic YBaMn_2O_5 have been described. The relatively small size of Y^{3+} makes the Mn–O–Mn bond angle within the basal plane deviate from 180° , which in turn imposes a reduction in the e_g -like electron-band width. The charge- and orbital-ordering features are believed to result from this perturbation of the e_g -like orbitals.

From gradient-corrected full-potential density-functional calculations one can reliably predict excited state properties such as XES, XANES, XPS, UPS, and BIS for magnetic oxides. This approach can be used to explain the origin of features in the experimentally observed spectra. Also, the degree of correlation effects present in solids can be understood by comparing the experimental spectra directly with corresponding theoretical spectra rather than with the calculated broadened density of states.

Using spin-polarized relativistic full-potential calculations we have demonstrated that band theory gives a completely satisfactory description of magneto-optical spectra for transition-metal compounds. In general large exchange- and spin-orbit splitting gives large magneto-optical effect. As finer features of band structure are involved in interband transitions, simple “rule of thumb” cannot be applied to predict magneto-optical materials useful in a specific energy range, but the present type of theoretical approach can be used to predict potential magneto-optical materials for application in the technology of erasable high-density data storage.

From ab initio frozen-phonon calculations one can reliably predict the zone boundary phonons such as infra-red- and Raman-active phonons as shown for the calculation of Raman-active phonon frequencies for superconducting and nonsuperconducting RT_2B_2C compounds. However, with regard to computational efficiency and even accessibility there are severe restrictions to this approach. Phonons with a low-symmetry wave-vector will generate a large super cell. As the computational effort to perform self-consistent band-structure calculations at one displacement pattern roughly scales with the number of atoms to the third power this approach is largely limited to high-symmetry phonons. To overcome this limitations one can use the linear-response formalism where the conventional frozen-phonon technique is coupled to concepts of first-order perturbation theory. Raman spectra can be calculated directly from frozen-phonon ab initio band-structure results (where the Raman intensity is expressed

by fluctuations of dielectric functions) and we have predicted the Raman spectrum for superconducting $\text{YNi}_2\text{B}_2\text{C}$ according to this approach.

Acknowledgments

A large part of the work described here was performed in collaboration with colleagues and inspired by several discussions. In particular P.R. wishes to thank O. Eriksson, L. Nordström, A. Delin, L. Fast, P.A. Korzhavyi, J.M. Wills, P. Blaha, B. Johansson, C. Ambrosch-Draxl, and S. Auluck. The present work was supported by the Research Council of Norway.

References

- [1] H. Hohenberg, W. Kohn, *Phys. Rev.* 136 (1964) 864.
- [2] W. Kohn, L.J. Sham, *Phys. Rev.* 140 (1965) 1133.
- [3] A.J. Maeland, in: M. Peruzzini, R. Poli (Eds.), *Recent Advances in Hydride Chemistry*, Elsevier, Amsterdam, 2001, p. 531.
- [4] L. Schlapbach, F. Meli, A. Züttel, in: J.H. Westbrook, R.L. Fleischer (Eds.), *Intermetallic Compounds: Practice*, Vol. 2, Wiley, New York, 1994, p. 475.
- [5] D.G. Westlake, *J. Less Common Met.* 103 (1984) 203.
- [6] A.C. Switendick, *Z. Phys. Chem.* 117 (1979) 89.
- [7] B.K. Rao, P. Jena, *Phys. Rev. B* 31 (1985) 6726.
- [8] P. Ravindran, P. Vajeeston, R. Vidya, A. Kjekshus, H. Fjellvåg, *Phys. Rev. Lett.* 89 (2002) 106403.
- [9] K. Ghoshray, B. Bandyopadhyay, M. Sen, A. Ghoshray, N. Chatterjee, *Phys. Rev. B* 47 (1993) 8277.
- [10] M. Sen, A. Ghoshray, K. Ghoshray, S. Sil, N. Chatterjee, *Phys. Rev. B* 53 (1996) 14345.
- [11] V.A. Yartys, R.V. Denys, B.C. Hauback, H. Fjellvåg, I.I. Bulyk, A.B. Riabov, Ya.M. Kalychak, *J. Alloys Compd.* 330–332 (2002) 132.
- [12] K. Yvon, P. Fischer, in: L. Schlapbach (Ed.), *Hydrogen in Intermetallics*, Springer, Berlin, 1988.
- [13] A. Delin, B. Johansson, *J. Magn. Magn. Mater.* 177–181 (1998) 373.
- [14] P. Vajeeston, R. Vidya, P. Ravindran, H. Fjellvåg, A. Kjekshus, A. Skjeltorp, *Phys. Rev. B* 65 (2002) 075101.
- [15] R. Dronskowski, P.E. Blöchl, *J. Phys. Chem.* 97 (1993) 8617.
- [16] O.K. Andersen, *Phys. Rev. B* 12 (1975) 3060; O.K. Andersen, O. Jepsen, *Phys. Rev. Lett.* 53 (1984) 2571; H.L. Skriver, *The LMTO Method*, Springer, Heidelberg, 1984.
- [17] G. Krier, O. Jepsen, A. Burkhardt, O.K. Andersen, *Tight Binding LMTO-ASA Program Version 4.7*, Stuttgart, Germany, 2000.
- [18] P. Vajeeston, P. Ravindran, R. Vidya, A. Kjekshus, H. Fjellvåg, V.A. Yartys, *Phys. Rev. B* 67 (2003) 014101.
- [19] M. Sen, S. Giri, K. Ghoshray, G. Bandyopadhyay, G. Ghoshray, N. Chatterjee, *Solid State Commun.* 89 (1994) 327.
- [20] A. Savin, R. Nesper, S. Wengert, T. Fässler, *Angew. Chem. Int. Ed. Engl.* 36 (1997) 1809.
- [21] A.L. Ruoff, H. Xia, H. Luo, Y.K. Vohra, *Rev. Sci. Instrum.* 61 (1990) 3830.
- [22] W.B. Holzapfel, *Rep. Prog. Phys.* 59 (1996) 29.
- [23] R.J. Hemley, N.W. Ashcroft, *Phys. Today* 51 (1998) 26.
- [24] T. Suski, W. Paul (Eds.), *High Pressure in Semiconductor Physics I*, Vol. 54, Academic Press, London, 1998.
- [25] Y. Chen, J.S. Williams, *J. Alloys Compd.* 217 (1995) 181.
- [26] J.P. Bastide, B. Bonnetot, J.M. Letoffe, P. Claudy, *Mat. Res. Bull.* 15 (1980) 1215.
- [27] M. Bortz, B. Bertheville, G. Böttger, K. Yvon, *J. Alloys Compd.* 287 (1999) L4.
- [28] J.E. Lowther, J.K. Dewhurst, J.M. Leger, J. Haines, *Phys. Rev. B* 60 (1999) 14485; J. Haines, J.M. Léger, O. Schulte, *J. Phys.: Condens. Matter* 8 (1996) 1631.
- [29] P. Vajeeston, P. Ravindran, A. Kjekshus, H. Fjellvåg, *Phys. Rev. Lett.* 89 (2002) 175506.
- [30] J.P. Perdew, in: P. Ziesche, H. Eschrig (Eds.), *Electronic Structure of Solids*, Akademie, Berlin, 1991, p. 11; J.P. Perdew, K. Burke, Y. Wang, *Phys. Rev. B* 54 (1996) 16533; J.P. Perdew, K. Burke, M. Ernzerhof, *Phys. Rev. Lett.* 77 (1996) 3865.
- [31] P.E. Blöchl, *Phys. Rev. B* 50 (1994) 17953; G. Kresse, J. Joubert, *Phys. Rev. B* 59 (1999) 1758.
- [32] J. Haines, J.M. Leger, O. Schulte, *J. Phys.: Condens. Matter* 8 (1996) 1631.
- [33] L.S. Dubrovinsky, N.A. Dubrovinskaia, V. Swamy, J. Muscat, N.M. Harrison, R. Ahuja, B. Holm, B. Johansson, *Nature (London)* 410 (2001) 653; N.A. Dubrovinskaia, L.S. Dubrovinsky, R. Ahuja, V.B. Prokopenko, V. Dmitriev, J.P. Weber, J.M. Osirio-Guillen, B. Johansson, *Phys. Rev. Lett.* 87 (2001) 275501.
- [34] P. Vajeeston, P. Ravindran, R. Vidya, H. Fjellvåg, A. Kjekshus, *Appl. Phys. Lett.* 82 (2003) 2257.
- [35] M.J. Mehl, B.M. Klein, D.A. Papaconstantopoulos, in: J.H. Westbrook, R.L. Fleischer (Eds.), *Intermetallic Compounds: Principles*, Vol. 1, Wiley, New York, 1994, p. 195.
- [36] P. Ravindran, L. Fast, P.A. Korzhavyi, B. Johansson, J.M. Wills, O. Eriksson, *J. Appl. Phys.* 84 (1998) 4891.
- [37] G. Kresse, J. Hafner, *Phys. Rev. B* 47 (1993) 558; G. Kresse, J. Furthmüller, *Comput. Mater. Sci.* 6 (1996) 15.
- [38] P. Ravindran, P. Vajeeston, R. Vidya, A. Kjekshus, H. Fjellvåg, *Phys. Rev. B* 64 (2001) 224509.
- [39] K. Tanaka, K. Okamoto, H. Inui, Y. Minonishi, M. Yamaguchi, M. Koiwa, *Phil. Mag. A* 73 (1996) 1475.
- [40] D.M. Ceperly, B.J. Alder, *Phys. Rev. Lett.* 45 (1980) 566; J.P. Perdew, A. Zunger, *Phys. Rev. B* 23 (1981) 5048.
- [41] J.P. Perdew, J.A. Chevary, S.H. Vosko, K.A. Jackson, M.R. Pederson, D.J. Singh, C. Fiolhais, *Phys. Rev. B* 46 (1992) 6671; Y. Wang, J.P. Perdew, *Phys. Rev. B* 44 (1991) 13298.
- [42] J.G. Bednorz, K.A. Müller, *Z. Phys. B* 64 (1986) 189.
- [43] R. von Helmolt, J. Wecker, B. Holzapfel, L. Shultz, K. Samwer, *Phys. Rev. Lett.* 71 (1993) 2331.
- [44] G. Pari, S.M. Jaya, G. Subramoniam, R. Asokamani, *Phys. Rev. B* 51 (1995) 16575.
- [45] Z. Yang, L. Ye, X. Xie, *J. Phys. Cond. Matt.* 12 (2000) 2737.
- [46] V.I. Anisimov, J. Zaanen, O.K. Andersen, *Phys. Rev. B* 44 (1991) 943.
- [47] I.V. Solovyev, P.H. Dederichs, V.I. Anisimov, *Phys. Rev. B* 50 (1994) 16861.
- [48] S. Bouarab, A. Vega, M.A. Khan, *Phys. Rev. B* 54 (1996) 11271.
- [49] H. Sawada, Y. Morikawa, K. Tarakura, N. Hamada, *Phys. Rev. B* 56 (1997) 12154.
- [50] J.B. Goodenough, *Phys. Rev.* 100 (1955) 564.
- [51] P. Ravindran, H. Fjellvåg, A. Kjekshus, A. Delin, O. Eriksson, *Phys. Rev. B* 65 (2002) 064445.
- [52] T. Saitoh, A.E. Bocquet, T. Mizokawa, H. Namatame, A. Fujimori, M. Abbate, Y. Takeda, M. Takano, *Phys. Rev. B* 51 (1995) 13942.
- [53] R. Mahendiran, S.K. Tiwary, A.K. Raychaudhuri, T.V. Ramakrishnan, R. Mahesh, N. Rangavittal, C.N.R. Rao, *Phys. Rev. B* 53 (1996) 3348.
- [54] G.H. Jonker, *Physica* 20 (1954) 1118.

- [55] T. Arima, Y. Tokura, J.B. Torrance, *Phys. Rev. B* 48 (1993) 17006.
- [56] Z. Yang, Z. Huang, L. Ye, X. Xie, *Phys. Rev. B* 60 (1999) 15674.
- [57] I.V. Solovyev, N. Hamada, K. Terakura, *Phys. Rev. B* 53 (1996) 7158.
- [58] T. Mizokawa, A. Fujimori, *Phys. Rev. B* 54 (1996) 5368.
- [59] S. Satpathy, Z.S. Popovic, F.R. Vakajlovic, *Phys. Rev. Lett.* 76 (1996) 960.
- [60] P. Ravindran, A. Delin, R. Ahuja, B. Johansson, S. Auluck, J.M. Wills, O. Eriksson, *Phys. Rev. B* 56 (1997) 6851.
- [61] M.T. Kostyshin, V.S. Kostko, I.Z. Indutnyi, V.M. Kosarev, *Opt. Spectrosc.* 52 (1982) 108.
- [62] I.S. Gorbun, V.F. Gorchin, T.N. Sushevich, *Sov. Phys. Solid State* 18 (1976) 1220.
- [63] M. Fujita, K. Hayakawa, K. Fukui, M. Kitaura, H. Nakagawa, T. Miyanaga, *J. Phys. Soc. Jpn.* 65 (1996) 605.
- [64] P. Ravindran, P.A. Korzhavyi, H. Fjellvåg, A. Kjekshus, *Phys. Rev. B* 60 (1999) 16423.
- [65] S. Yamaguchi, Y. Okimoto, H. Taniguchi, Y. Tokura, *Phys. Rev. B* 53 (1996) R2926.
- [66] R.M. Dreizler, E.K.U. Gross, *Density Functional Theory*, Springer, Berlin, 1990.
- [67] F. Bechstedt, R. Del Sole, *Phys. Rev. B* 38 (1988) 7710.
- [68] Y. Okimoto, T. Katsufuji, T. Ishikawa, A. Urushibara, T. Arima, Y. Tokura, *Phys. Rev. Lett.* 75 (1995) 109.
- [69] W.E. Pickett, D.J. Singh, *Phys. Rev. B* 53 (1996) 1146.
- [70] P. Mahadevan, N. Shanthi, D.D. Sarma, *J. Phys.: Condens. Matter* 9 (1997) 3129.
- [71] W.C. Koehler, E.O. Wollan, *J. Phys. Chem. Solids* 2 (1957) 100.
- [72] V.G. Zubkov, G.V. Bazuev, V.A. Perelyaev, G.P. Shveikin, *Sov. Phys. Solid State* 15 (1973) 1079.
- [73] P. Bordet, C. Chaillout, M. Marezio, Q. Haung, A. Santoro, S.-W. Cheong, H. Takagi, C.S. Oglesby, B. Batlogg, *J. Solid State Chem.* 106 (1993) 253.
- [74] P. Dougier, P. Hagenmuller, *J. Solid State Chem.* 11 (1974) 177.
- [75] A. Svane, O. Gunnarsson, *Phys. Rev. Lett.* 65 (1990) 1148.
- [76] E.K.U. Gross, W. Khon, *Adv. Quant. Chem.* 21 (1990) 255.
- [77] V.I. Anisimov, A.I. Poteryaev, M.A. Korotin, A.O. Anokhin, G. Kotliar, *J. Phys.: Condens. Matter* 9 (1997) 7359.
- [78] Y. Maeno, H. Hashimoto, K. Yoshida, S. Nishizaki, T. Fujita, J.G. Bednorz, F. Lichtenber, *Nature* 372 (1995) 532.
- [79] A. Callaghan, C.W. Moeller, R. Ward, *Inorg. Chem.* 5 (1966) 1572.
- [80] P. Kostic, Y. Okada, N.C. Collins, Z. Schlesinger, J.W. Reiner, L. Klein, A. Kapitulnik, T.H. Geballe, M.R. Beasley, *Phys. Rev. Lett.* 81 (1998) 2498.
- [81] J.M. Longo, P.M. Racciah, J.B. Goodenough, *J. Appl. Phys.* 39 (1968) 1327.
- [82] J.L. Martinez, C. Prieto, J. Rodriguez-Carvajal, A. de Andres, M. Vallet-Regi, J.M. Gonzalez-Calbet, *J. Magn. Magn. Mater.* 140–144 (1995) 179.
- [83] T. Kiyama, K. Yoshimura, K. Kosuge, H. Mitamura, T. Goto, *J. Phys. Soc. Jpn.* 68 (1999) 3372.
- [84] K. Yoshimura, T. Imai, T. Kiyama, K.R. Thurber, A.W. Hunt, K. Kosuge, *Phys. Rev. Lett.* 83 (1999) 4397.
- [85] T.C. Gibb, R. Greatrex, N.N. Greenwood, P. Kaspi, *J. Chem. Soc., Dalton Trans.* 3 (1973) 1253.
- [86] I.I. Mazin, D.J. Singh, *Phys. Rev. B* 56 (1997) 2556.
- [87] I. Felner, I. Nowik, I. Bradaric, M. Gospodinov, *Phys. Rev. B* 62 (2000) 11332.
- [88] P. Ravindran, R. Vidya, P. Vajeeston, A. Kjekshus, H. Fjellvåg, B.C. Hauback, *Solid State Commun.* 124 (2002) 293.
- [89] R. Vidya, P. Ravindran, A. Kjekshus, H. Fjellvåg, B.C. Hauback (unpublished).
- [90] F. Fukunaga, N. Tsuda, *J. Phys. Soc. Jpn.* 63 (1994) 3798.
- [91] H. Eschrig, *The Fundamentals of Density Functional Theory*, Teubner, Dortmund, 1996.
- [92] A. Gonis, N. Kioussis, M. Ciftan (Eds.), *Correlation Effects and Materials Properties*, Kluwer Academic, New York, 1999.
- [93] M.S.S. Brooks, *Physica B* 130 (1985) 6; O. Eriksson, M.S.S. Brooks, B. Johansson, *Phys. Rev. B* 41 (1990) 7311.
- [94] H.J.F. Jansen, *J. Appl. Phys.* 67 (1990) 4555.
- [95] O. Eriksson, B. Johansson, R.C. Albers, A.M. Boring, M.S.S. Brooks, *Phys. Rev. B* 42 (1990) 2707.
- [96] O. Eriksson, M.S.S. Brooks, B. Johansson, *Phys. Rev. B* 41 (1990) 9087.
- [97] G. Racah, *Phys. Rev.* 61 (1942) 186.
- [98] M.S.S. Brooks, P.J. Kelly, *Phys. Rev. Lett.* 51 (1983) 1708.
- [99] F.A. Wedgwood, M. Kuznietz, *J. Phys. C* 5 (1972) 3012.
- [100] G.H. Lander, in: W.D. Corner, B.K. Tanner (Eds.), *Rare Earths and Actinides 1977*, Institute of Physics, Bristol, 1978, p. 173.
- [101] P.S. Papamantellos, P. Fischer, A. Niggli, E. Kaldis, V. Hildebrandt, *J. Phys. C* 7 (1974) 2023.
- [102] H.R. Ott, J.K. Kjems, F. Hulliger, *Phys. Rev. Lett.* 42 (1979) 1378.
- [103] H. Sakurai, H. Hashimoto, A. Ochiai, T. Suzuki, M. Ito, F. Itoh, *J. Phys.: Condens. Matter* 7 (1995) L599.
- [104] R.D. Shannon, *Acta. Crystallogr. Sec. A* 32 (1976) 751.
- [105] J.C. Lodder, *Mater. Res. Bull.* 20 (1995) 59; J.L. Simonds, *Phys. Today* 48 (1995) 26.
- [106] P. Ravindran, A. Kjekshus, H. Fjellvåg, P. James, L. Nordström, B. Johansson, O. Eriksson, *Phys. Rev. B* 63 (2001) 144409.
- [107] J. Trygg, B. Johansson, O. Eriksson, J.M. Wills, *Phys. Rev. Lett.* 75 (1995) 2871.
- [108] J.M. Wills, O. Eriksson, M. Alouani, D.L. Price, in: H. Dreyse (Ed.), *Electronic Structure and Physical Properties of Solids*, Springer, Berlin, 2000, p. 148; J.M. Wills, B.R. Cooper, *Phys. Rev. B* 36 (1987) 3809; D.L. Price, B.R. Cooper, *Phys. Rev. B* 39 (1989) 4945.
- [109] A. Sakuma, *J. Phys. Soc. Jpn.* 63 (1994) 3053.
- [110] I.V. Solovyev, P.H. Dederichs, I. Mertig, *Phys. Rev. B* 52 (1995) 13419.
- [111] V.V. Maykov, A. Ye Yermakov, G.V. Ivanov, V.I. Khrabrov, L.M. Magat, *Phys. Met. Metallogr.* 67 (1989) 76.
- [112] P. Brissoneau, A. Blanford, H. Bartolin, *IEEE Trans. Magn. MAG-2* (1966) 479.
- [113] P.M. Oppeneer, *J. Magn. Magn. Mater.* 188 (1998) 275.
- [114] V.G. Pyn'ko, L.V. Zhivayeva, N.A. Ekonomov, A.S. Komalov, N.N. Yevtikhiyev, A.R. Krebs, *Phys. Met. Metallogr.* 45 (1979) 179.
- [115] P. Kamp, A. Marty, B. Gilles, R. Hoffmann, S. Marchesini, M. Belokhovskiy, C. Boeglin, H.A. Dürr, S.S. Dhesi, G. Van der Laan, A. Rogalev, *Phys. Rev. B* 59 (1999) 1105.
- [116] L.M. Magat, A. Syermolenko, G.V. Ivanova, *Fiz. Metal. Metalloved.* 26 (1968) 511.
- [117] Y.-S. Kim, S.-C. Shin, *Phys. Rev. B* 59 (1999) R6597; S.-C. Shin, G. Srinivas, Y.-S. Kim, M.-G. Kim, *Appl. Phys. Lett.* 73 (1998) 393.
- [118] M.B. Stearns, in: H.P.J. Wijn (Ed.), *3d, 4d, 5d Elements, Alloys and Compounds*, Landolt-Börnstein, New Series, Vol. 19, Group 3, Springer, Berlin, 1986.
- [119] R.R. Heikes, R.C. Miller, R. Mazelsky, *Physica (Amsterdam)* 30 (1964) 1600.
- [120] G.H. Jonker, *J. Appl. Phys.* 37 (1966) 1424.
- [121] P.M. Racciah, J.B. Goodenough, *Phys. Rev.* 155 (1967) 932.
- [122] K. Asai, O. Yokokura, N. Nishimori, H. Chou, J.M. Tranquada, G. Shirane, S. Higuchi, Y. Okajima, K. Kohn, *Phys. Rev. B* 50 (1994) 3025.

- [123] M. Abbate, J.C. Fuggle, A. Fujimori, L.H. Tjeng, C.T. Chen, R. Potze, G.A. Sawatzky, H. Eisaki, S. Uchida, *Phys. Rev. B* 47 (1993) 16124.
- [124] S.R. Barman, D.D. Sarma, *Phys. Rev. B* 49 (1994) 13979.
- [125] M.A. Korotin, S.Yu. Ezhov, I.V. Solovyev, V.I. Anisimov, D.I. Khomskii, G.A. Sawatzky, *Phys. Rev. B* 54 (1996) 5309.
- [126] T. Saitoh, T. Mizokawa, A. Fujimori, M. Abbate, Y. Takeda, M. Takano, *Phys. Rev. B* 55 (1997) 4257.
- [127] K. Asai, A. Yoneda, O. Yokokura, J.M. Tranquada, J.M. Shirane, K. Kohn, *J. Phys. Soc. Jpn.* 67 (1998) 290.
- [128] C.S. Naiman, R. Gilmore, B. Dabartolo, A. Linz, R. Santoro, *J. Appl. Phys.* 36 (1965) 1044.
- [129] M.A.S. Rodriguez, J.B. Goodenough, *J. Solid State Chem.* 116 (1995) 224.
- [130] M. Itoh, M. Sugahara, I. Tatori, K. Motoya, *J. Phys. Soc. Jpn.* 64 (1995) 3967.
- [131] K. Asai, O. Yokokura, M. Suzuki, T. Naka, T. Matsumoto, H. Takahashi, N. Mori, K. Kohn, *J. Phys. Soc. Jpn.* 66 (1997) 967.
- [132] R. Marx, *Phys. Stat. Sol. B* 99 (1980) 555.
- [133] M. Itoh, I. Tatori, *J. Magn. Magn. Mater.* 140–144 (1995) 2145.
- [134] M. Itoh, M. Mori, M. Sugahara, T. Yamaguchi, Y. Ueda, *Physica B* 230–232 (1997) 756.
- [135] R.H. Potze, G.A. Sawatzky, M. Abbate, *Phys. Rev. B* 51 (1995) 11501.
- [136] S. Stölen, F. Grönvold, H. Brinks, T. Atake, H. Mori, *Phys. Rev. B* 55 (1997) 1413.
- [137] R. Caciuffo, D. Rinaldi, G. Barucca, J. Mira, J. Rivas, M.A.S. Rodriguez, P.G. Radaelli, D. Frorani, J.B. Goodenough, *Phys. Rev. B* 59 (1999) 1068.
- [138] P. Ravindran, H. Fjellvåg, A. Kjekshus, P. Blaha, K. Schwarz, J. Luitz, *J. Appl. Phys.* 91 (2002) 291.
- [139] K. Schwarz, P. Mohn, *J. Phys. F: Met. Phys.* 14 (1984) L129.
- [140] V.L. Moruzzi, P.M. Marcus, K. Schwarz, P. Mohn, *Phys. Rev. B* 34 (1986) 1784.
- [141] T. Goto, H. Aruga Katori, T. Sakakibara, H. Mitamura, K. Fukamichi, K. Murata, *J. Appl. Phys.* 76 (1994) 6683.
- [142] H. Takahashi, F. Munakata, M. Yamanaka, *Phys. Rev. B* 53 (1996) 3731.
- [143] M. Cyrot, D. Gignoux, F. Givord, M. Lavagna, *J. Phys. Coll.* C5 40 (1979) 171.
- [144] S.T. Liu, Y. Wu, Y.Q. Jia, *J. Alloys Compd.* 200 (1993) 171.
- [145] V.G. Bhide, D.S. Rajoria, G.R. Rao, C.N.R. Rao, *Phys. Rev. B* 6 (1972) 1021.
- [146] G.H. Jonker, J.H. van Santen, *Physica (Amsterdam)* 19 (1953) 120.
- [147] P.M. Raccach, J.B. Goodenough, *J. Appl. Phys.* 39 (1968) 1209.
- [148] V.G. Bhide, D.S. Rajoria, C.N.R. Rao, G.R. Rao, V.G. Jadhao, *Phys. Rev. B* 12 (1975) 2832.
- [149] Y. Tokura, Y. Okimoto, S. Yamaguchi, H. Taniguchi, T. Kimura, H. Takagi, *Phys. Rev. B* 58 (1998) R1699.
- [150] M. Itoh, J. Natori, *J. Phys. Soc. Jpn.* 64 (1995) 970.
- [151] M.A. Senaris-Rodriguez, J.B. Goodenough, *J. Solid State Chem.* 118 (1995) 323.
- [152] M. Magnuson, S.M. Butorin, J. Nordgren, P. Ravindran (unpublished).
- [153] C.N.R. Rao, B. Raveau (Eds.), *Colossal Magnetoresistance, Charge Ordering and Related Properties of Manganese Oxides*, World Scientific, Singapore, 1998.
- [154] Y. Tokura (Ed.), *Colossal Magnetoresistive Oxides*, Gordon and Breach, Amsterdam, 2000.
- [155] T.A. Kaplan, S.D. Mahanti (Eds.), *Physics of Manganites*, Kluwer Academic, New York, 1998.
- [156] A.J. Millis, P.B. Littlewood, B.I. Shraiman, *Phys. Rev. Lett.* 74 (1995) 5144.
- [157] H. Röder, J. Zhang, A.R. Bishop, *Phys. Rev. Lett.* 76 (1996) 1356.
- [158] R. Vidya, P. Ravindran, A. Kjekshus, H. Fjellvåg, *Phys. Rev. B* 65 (2002) 144422.
- [159] F. Millange, E. Suard, V. Caignaert, B. Raveau, *Mat. Res. Bull.* 34 (1999) 1.
- [160] J.B. Goodenough, in: H. Reiss (Ed.), *Progress in Solid State Chemistry*, Vol. 5, Pergamon Press, Oxford, 1971.
- [161] J.B. Goodenough, *Magnetism and the Chemical Bond*, Wiley, New York, 1963.
- [162] J.B. Goodenough, *Phys. Rev.* 100 (1955) 564; J. Kanamori, *J. Phys. Chem. Solids* 10 (1959) 87.
- [163] H. Kuwahara, Y. Tomioka, A.M. Asamitsu, Y. Tokura, *Science* 270 (1995) 961.
- [164] Y. Moritomo, H. Kuwahara, Y. Tomioka, Y. Tokura, *Phys. Rev. B* 55 (1997) 7549.
- [165] V. Kiryukhin, D. Casa, J.P. Hill, B. Keimer, A. Vigliante, Y. Tomioka, Y. Tokura, *Nature* 386 (1997) 813.
- [166] Y. Murakami, H. Kawada, H. Kuwata, M. Tanaka, T. Arima, Y. Moritomo, Y. Tokura, *Phys. Rev. Lett.* 80 (1998) 1932.
- [167] Y. Tokura, H. Kuwahara, Y. Moritomo, Y. Tomioka, A. Asamitsu, *Phys. Rev. Lett.* 76 (1996) 3184.
- [168] Y. Tokura, N. Nagaosa, *Science* 288 (2000) 462.
- [169] H. Sawada, K. Terakura, *Phys. Rev. B* 58 (1998) 6831.
- [170] S.-W. Cheong, in: C.N.R. Rao, B. Raveau (Eds.), *Colossal Magnetoresistance, Charge Ordering and Related Properties of Manganese Oxides*, World Scientific, Singapore, 1998, p. 241.
- [171] A. Neckel, K. Schwarz, R. Eibler, P. Rastl, *Microchim. Acta Suppl.* 6 (1975) 257.
- [172] P. Blaha, K. Schwarz, J. Luitz, WIEN97, Vienna University of Technology, Vienna, Austria, 1997 [Improved and updated version of the original copyrighted WIEN code, which was published by P. Blaha, K. Schwarz, P. Sorantin, S.B. Trickey, *Comput. Phys. Commun.* 59 (1990) 399].
- [173] G. Subias, J. Garcia, J. Blasco, M.G. Proietti, *Phys. Rev. B* 58 (1998) 9287.
- [174] F. Bridges, C.H. Booth, G.H. Kwei, J.J. Neumeier, G.A. Sawatzky, *Phys. Rev. B* 61 (2000) R9237.
- [175] M. Croft, D. Sills, M. Greenblatt, C. Lee, S.-W. Cheong, K.V. Ramanujachary, D. Tran, *Phys. Rev. B* 55 (1997) 8726.
- [176] J.-H. Park, C.T. Chen, S.-W. Cheong, W. Bao, G. Meigs, V. Chakarian, Y.U. Idzerda, *Phys. Rev. Lett.* 76 (1996) 4215.
- [177] M. Abbate, G. Zampieri, F. Prado, A. Caneiro, A.R.B. Castro, *Solid State Commun.* 111 (1999) 437.
- [178] H. Winter, P.J. Durham, G.M. Stocks, *J. Phys. F: Met. Phys.* 14 (1984) 1047.
- [179] J. Redinger, P. Marksteiner, P. Weinberger, *Z. Phys. B* 63 (1986) 321.
- [180] M.V.R. Rao, V.G. Sathe, D. Sornadurai, B. Panigrahi, T. Shripathi, *J. Phys. Chem. Solids* 62 (2001) 797.
- [181] N.V. Smith, *Phys. Rev. B* 3 (1971) 1862.
- [182] H. Ehrenreich, M.H. Cohen, *Phys. Rev.* 115 (1959) 786.
- [183] M. Alouani, J.M. Wills, *Phys. Rev. B* 54 (1996) 2480; R. Ahuja, S. Auluck, J.M. Wills, M. Alouani, B. Johansson, O. Eriksson, *Phys. Rev. B* 55 (1997) 4999.
- [184] P. Ravindran, A. Delin, B. Johansson, O. Eriksson, J.M. Wills, *Phys. Rev. B* 59 (1999) 1776.
- [185] J.H. Jung, K.H. Kim, K.J. Eom, T.W. Noh, E.J. Choi, J. Yu, Y.S. Kwon, Y. Chung, *Phys. Rev. B* 55 (1997) 15489.
- [186] K. Takenaka, K. Iida, Y. Sawaki, S. Sugai, Y. Moritomo, A. Nakamura, *J. Phys. Soc. Jpn.* 68 (1999) 1828.
- [187] P. Ravindran, A. Delin, P. James, B. Johansson, J.M. Wills, R. Ahuja, O. Eriksson, *Phys. Rev. B* 59 (1999) 15680.
- [188] M. Faraday, *Phil. Trans. Roy. Soc.* 136 (1846) 1.

- [189] J. Schoenes, in: *Materials Science and Technology*, Vol. 3A, Electronic and Magnetic Properties of Metals and Ceramics, VCH, New York, 1992;
K.H.K. Buschow, in: E.P. Wohlfarth, K.H.J. Buschow (Eds.), *Ferromagnetic Materials*, Vol. 4, Elsevier, Amsterdam, 1988 (Chapter 5).
- [190] P.J. Grundy, in: *Materials Science and Technology*, Vol. 3B, Electronic and Magnetic Properties of Metals and Ceramics, VCH, FRG, 1994.
- [191] P.M. Oppeneer, J. Sticht, F. Herman, *J. Magn. Soc. Jpn.* 15 (S1) (1991) 73.
- [192] S.V. Halilov, R. Feder, *Solid State Commun.* 88 (1993) 749.
- [193] G.Y. Guo, H. Ebert, *Phys. Rev. B* 50 (1994) 10377.
- [194] T. Gasche, Ph.D. Thesis, Uppsala University, 1994.
- [195] J. Schoenes, in: A.J. Freeman, G.H. Lander (Eds.), *Handbook of the Physics and Chemistry of the Actinides*, Vol. 1, North-Holland, Amsterdam, 1984, p. 341.
- [196] F.J. Kahn, P.S. Pershan, J.P. Remeika, *Phys. Rev.* 186 (1969) 891.
- [197] W. Reim, J. Schoenes, in: K.H.K. Buschow, E.P. Wohlfarth (Eds.), *Ferromagnetic Materials*, Vol. 5, Elsevier, Amsterdam, 1990.
- [198] P. Drude, *Ann. Phys. (Leipzig)* 1 (1900) 566;
P. Drude, *Ann. Phys. (Leipzig)* 3 (1900) 369.
- [199] P. Mohn, P. Blaha, K. Schwarz, *J. Magn. Magn. Mater.* 140–144 (1995) 183.
- [200] G.Q. Di, S. Uchiyama, *J. Appl. Phys.* 75 (1994) 4270.
- [201] D. Weller, in: H. Ebert, G. Schütz (Eds.), *Spin-Orbit Influenced Spectroscopies of Magnetic Solids*, Springer, Berlin, 1996, p. 1.
- [202] A. Cebollada, D. Weller, J. Sticht, G.R. Harp, R.F.C. Farrow, R.F. Marks, R. Savoy, J.C. Scott, *Phys. Rev. B* 50 (1994) 3419.
- [203] T. Sugimoto, T. Katayama, Y. Suzuki, T. Koide, T. Sidara, M. Yuri, A. Itoh, K. Kawanishi, *Phys. Rev. B* 48 (1993) 16432.
- [204] S.P. Lim, *J. Appl. Phys.* 81 (1997) 5426.
- [205] P.M. Oppeneer, V.N. Antonov, in: H. Ebert, G. Schütz (Eds.), *Spin-Orbit Influenced Spectroscopies of Magnetic Solids*, Springer, Berlin, 1996, p. 29.
- [206] P.N. Argyres, *Phys. Rev.* 97 (1955) 334.
- [207] G.H.O. Daalderop, P.J. Kelly, M.F.H. Schuurmans, *Phys. Rev. B* 44 (1991) 12054.
- [208] Y. Wu, J. Stöhr, B.D. Hermsmeier, M.G. Samant, D. Weller, *Phys. Rev. Lett.* 69 (1992) 2307.
- [209] J.W. Cable, E.O. Wollan, W.C. Koehler, *Phys. Rev.* 138 (1965) A755.
- [210] H. Ebert, *Rep. Prog. Phys.* 59 (1996) 1665.
- [211] G. Armelles, D. Weller, B. Rellinghaus, R.F.C. Farrow, M.F. Toney, P. Caro, A. Cebollada, M.I. Alonso, *IEEE Trans. Magn.* 33 (1997) 3220.
- [212] K. Sato, Y. Tosaka, H. Ikekame, M. Watanabe, K. Takamashi, H. Fujimori, *J. Magn. Magn. Mater.* 148 (1995) 206.
- [213] V.G. Pyn'ko, L.V. Zhivayeva, N.A. Ekonomov, A.S. Komalov, N.N. Yevtkhiyev, A.R. Krebs, *Phys. Met. Metallogr.* 45 (1978) 179.
- [214] E. Feldtkeller, *IEEE Trans. Magn.* MAG-8 (1972) 481;
D. Chen, G.M. Otto, F.M. Schmit, *IEEE Trans. Magn.* MAG-9 (1973) 66.
- [215] J.T. Devreese, V.E. van Doren, P.E. van Camp (Eds.), *Ab-initio Calculation of Phonon Spectra*, Plenum, New York, 1983.
- [216] C. Ambrosch-Draxl, R. Kouba, P. Knoll, *Z. Phys. B* 104 (1995) 687.
- [217] T. Siegrist, H.W. Zandbergen, R.J. Cava, J.J. Krajewski, W.F. Peck, *Nature (London)* 367 (1994) 254.
- [218] T. Siegrist, R.J. Cava, J.J. Krajewski, W.F. Peck, *J. Alloys Compd.* 216 (1994) 135.
- [219] A.K. Gangopadhyay, A.J. Schuetz, J. Schilling, *Physica C* 246 (1995) 317.
- [220] R. Weht, O.M. Cappannini, C.O. Rodriguez, N.E. Christensen, *Physica C* 260 (1996) 125.
- [221] J. Hartmann, F. Gompf, B. Renker, *J. Low Temp. Phys.* 105 (1996) 1629.
- [222] V.G. Hadjiev, L.N. Bozukov, M.G. Baychev, *Phys. Rev. B* 50 (1994) 16726.
- [223] A.P. Litvinchuk, L. Börjesson, N.X. Phuc, N.M. Hong, *Phys. Rev. B* 52 (1995) 6208.
- [224] H.J. Park, H.-S. Shin, H.G. Lee, I.S. Yang, W.C. Lee, B.K. Cho, P.C. Canfield, D.C. Johnston, *Phys. Rev. B* 53 (1996) 2237.
- [225] F. Gompf, W. Reichardt, H. Schober, B. Renker, M. Buchgeister, *Phys. Rev. B* 55 (1997) 9058.
- [226] Y. Okamoto, M. Saito, A. Oshiyama, *Phys. Rev. B* 56 (1997) R10016.
- [227] R. Kouba, C. Ambrosch-Draxl, *Z. Phys. B* 104 (1997) 777.
- [228] P. Ravindran, B. Johansson, O. Eriksson, *Phys. Rev. B* 58 (1998) 3381.
- [229] M. Cardona, in: M. Cardona, G. Guntherodt (Eds.), *Light Scattering in Solids II*, Vol. 50, Topics in Applied Physics Springer, Springer, Berlin, 1982.
- [230] P. Knoll, C. Ambrosch-Draxl, in: D. Mihailovic, G. Ruani, E. Kaldis, K.A. Müller (Eds.), *Anharmonic Properties of High- T_c cuprates*, World Scientific, Singapore, 1994, p. 220.
- [231] P. Ravindran, P. Puschnig, C. Ambrosch-Draxl, L. Nordström, A. Kjekshus, H. Fjellvåg, B. Johansson, *Phys. Rev. B* 67 (2003) 104507.